Special Issue on Selected Emerging Trends in Terahertz Science and Technology

Towards Passive Imaging With Uncooled, Low-NEP SiGe HBT Terahertz Direct Detectors

Marcel Andree, *Member, IEEE*, Janusz Grzyb, Holger Rücker, and Ullrich R. Pfeiffer, *Fellow, IEEE*

***Abstract*—This work focuses on a systematic analysis of the potential and limitations of modern SiGe HBT devices for broadband passive room-temperature detection in the lower THz range. Multiple necessary conditions need to be fulfilled to facilitate broadband passive imaging with a sufficiently low in-band NEP, which refer to various technology-driven device operation aspects, including the THz rectification process and low-frequency analysis. To properly understand and model the devices' internal parasitics in combination with antenna-detector co-design aspects, a simplified nonlinear high-frequency detector model was applied for the devices operating in the forward-active and saturation region (cold operation). The complete detector was implemented in a modern high-speed 130 nm SiGe HBT technology with $f_t/f_{\max}$ of 470/650 GHz. It comprises two orthogonal polarization paths within a single dual-polarization lens-coupled on-chip antenna to operate with unpolarized passive illumination. Due to an efficient antenna-circuit co-design, a close-to-optimum detector performance in a near-THz fractional bandwidth was achieved, as experimentally verified in free-space measurements with frequency-tunable coherent CW sources. The detector optical NEP for each polarization path was measured across 200–1000 GHz reporting state-of-the-art values of 2.3–23 pW/$\sqrt{\text{Hz}}$ (forward-active) and 4.3–45 pW/$\sqrt{\text{Hz}}$ (saturation). This, combined with the de-embedded equivalent noise bandwidth of 512 GHz around 430 GHz, allowed to demonstrate a 1-Hz defined NETD of 0.86 K and 2 K with a focussed cavity blackbody standard chopped mechanically at 1.5 kHz. By dual-channel operation, the NETD scaled down to 0.64 K, indicating near-zero noise correlation between both polarization paths.**

***Index Terms*—Direct detector, dual-polarization, noise equivalent power (NEP), noise equivalent temperature difference (NETD), onchip antenna, passive imaging, radiometry, SiGe HBT, submillimeter wave, terahertz (THz).**

Manuscript received 21 March 2024; revised 27 June 2024; accepted 17 July 2024. Date of publication 23 July 2024; date of current version 5 September 2024. This work was partially supported by the Deutsche Forschungsgemeinschaft (DFG, German Research Foundation) under Grant 287022738 (TRR 196 project C08) and under Grant 419161860 (DotSeven2IC). *(Corresponding author: Marcel Andree.)*

Marcel Andree, Janusz Grzyb, and Ullrich R. Pfeiffer are with the Institute of High-Frequency and Communication Technology, University of Wuppertal, D-42119 Wuppertal, Germany (e-mail: andree@uni-wuppertal.de).

Holger Rücker is with the IHP-Leibniz-Institut für Innovative Mikroelektronik, D-15236 Frankfurt (Oder), Germany.

Color versions of one or more figures in this article are available at https://doi.org/10.1109/TTHZ.2024.3432619.

Digital Object Identifier 10.1109/TTHZ.2024.3432619

I. Introduction

APART from astronomical imaging systems [1], security screening [2] belongs to the most relevant applications of total-power radiometers [3], [4] operating in the upper mmWave as well as submillimeter-wave bands below 1 THz. In this frequency range, most dielectric materials are optically transparent [5], thus allowing potentially efficient imaging of hidden objects. At the same time, an acceptable diffraction-limited spatial resolution can simultaneously be provided [6]. Total-power radiometers are ideal candidates for complete real-time passive imaging arrays as they do not require any LO signal distribution. However, compared to the infrared range, due to low total irradiance available below 1 THz [7], the radiometer temperature resolution, defined by the noise-equivalent temperature difference (NETD), becomes a challenging design goal, in particular for low-contrast (indoor) applications. Here, minimum NETD values below 1 K are typically seen as the threshold for an effective concealed object detection [8], [9]. At room temperatures, such NETD values are currently achievable with a limited-count of scanning arrays comprising LNA-preamplified detectors operating in the lower-end of the THz frequency range [10], [11], [12], [13], [14], [15], [16], [17], [18], [19], [20], [21] due to obvious limitations of the active technologies in use. In any other case, cryogenic cooling of the larger-format arrays of kinetic inductance bolometers and detectors (KID) [6], transition-edge sensors (TES) [22], [23], superconducting microbolometers [8], [9], [24], [25], and tunneling junctions [26] is normally exploited to reach passive operation.

The more widespread deployment of scalable low-power THz imaging arrays requires the use of more affordable, highly integrated technologies, ideally operated at room temperature. Full array scalability indirectly limits the pixel architecture to a simple antenna-coupled direct detector without preamplification, which is too expensive to implement in terms of power consumption and chip real-estate. Considering that state-of-the-art realistic room-temperature-referred optical noise equivalent power (NEP) values are in a few pW/$\sqrt{\text{Hz}}$-range not only for highly integrated silicon technologies [27], [28], [29], but also for III-V process options [30], [31], a sub-Kelvin NETD operation translates directly into the required RF noise-equivalent bandwidth of at least a few hundred GHz and, therefore, puts the antenna-detector codesign issues at the forefront of all design tasks [28], [32], [33], [34]. This critical design aspect is rarely addressed in detail as the current work is almost exclusively devoted to demonstrating lowest possible NEP values independent from RF operation bandwidth.

Among all available process options, silicon-integrated direct detectors are one of the main candidates for large-scale focal-plane array (FPA) implementation thanks to their capability of a single-chip integration with high-complexity readout electronics. Here, the main research effort focuses on the so-called self-mixing process in the cold-operated MOSFET channel [35], [36], [37], [38] which guarantees low-power dissipation. The reported state-of-the-art NEP values vary from 3.5 pW/$\sqrt{\mathrm{Hz}}$ to around 12–14 pW/$\sqrt{\mathrm{Hz}}$ across 300–850 GHz [29], [39], [40], [41], [42], [43]. Even though the rectification by a regular p-n junction or a Schottky barrier diode (SBD) [44], [45], [46] is well known and documented in the literature at THz frequencies with NEP widely ranging from 20 pW/$\sqrt{\mathrm{Hz}}$ to 56 pW/$\sqrt{\mathrm{Hz}}$ [32], [47], [48], the related THz detection with a SiGe HBT is not extensively studied in the literature [49], [50]. The lowest optical NEP values reported here change from 1.9 pW/$\sqrt{\mathrm{Hz}}$ at 292 GHz [27], [28], through 2.7 pW/$\sqrt{\mathrm{Hz}}$ at 476 GHz [51], to 16 pW/$\sqrt{\mathrm{Hz}}$ around 1 THz [52], and, therefore, they outperform those demonstrated for the MOSFET counterparts.

Irrespectively from the device option under consideration, broadband imaging with NETD below 1 K has so far only been reported with cooled microbolometers [6], [8], [9], [23] or III-V GaN HEMTs [30] but not with room-temperature operated, silicon-integrated THz direct detectors. Therefore, the main focus of this manuscript is a systematic analysis of the potential as well as the limitations of modern SiGe HBT devices for broadband passive room temperature detection in the lower THz range. In order to emphasize the importance of the contemporary technology scaling trends, the analysis is performed for the fastest currently available technology node, namely 130 nm with $f_t/f_{\max}$ of 470/650 GHz. To facilitate passive imaging, both large RF fractional operation bandwidth and a low in-band detector NEP are necessary conditions that need to be fulfilled. Considering a strong frequency dependence of the device inherent rectification potential, the antenna-detector co-design aspects with an in-depth understanding of the internal device parasitics become crucial for successful detector implementation. Equally important is proper modeling as well as experimental verification of the device low-frequency noise (LFN) components; even though the transistors are operated at low bias current densities, considerably below those corresponding to the maximum device speed. For large-format FPA arrangements, a total power dissipation appears as a critical design aspect. Here, a cold device operation, with no external collector voltage applied, may become viable. This bias range is commonly but misleadingly ignored in the foreseen frequency operation because of a low device speed in terms of $f_t/f_{\max}$ [53], [54], [55], [56], [57], [58].

The rest of this article is organized as follows. In Section II, a brief summary of the current state-of-the-art for the highly integrated direct detectors in the lower THz frequency range is presented, emphasizing various operation aspects relevant to passive imaging. Section III provides initial guidelines on the combined choice of detector circuit and antenna topology. In Section IV, all low-frequency aspects of detector operation will be discussed. This includes optimum bias conditions both for forward-active range as well as for saturation (cold operation), low-frequency noise analysis, and low-frequency responsivity constraints driven by technological aspects. Section V deals with all aspects of detector rectification process at THz frequencies, linking them with the internal device parasitics by means of a nonlinear high-frequency device model. Some selected antenna-detector co-design issues relevant for small form-factor but broadband operation with unpolarized light will be detailed in Section VI. The major characterization results performed with a set of CW RF power sources as well as with a reference cavity black-body standard are discussed in Sections VII and VIII. The initial passive imaging experiments are presented in Section IX. Finally, Section X concludes this article.

II. Toward Room Temperature Passive Imaging With Silicon-Integrated Direct Detectors

Considering that a radiometer operating in the Rayleigh–Jeans limit [4] is illuminated with an incoherent and spatially-distributed source with power spectral density given by $k_B T$ [32], [33], its absolute RF bandwidth becomes a key figure-of-merit toward maximizing the total radiometric response. In the lower limit of the considered 0.1–1 THz frequency band, the radiometer performance can still be boosted with LNA preamplification. Ideally, the far-out noise of a standalone power detector is, in this case, masked by the preceding LNA with sufficiently high gain and low NF, and the final NETD relates only to the LNA NF, its RF bandwidth, and integration time. With respect to that, III-V semiconductors, in particular InP, typically become the first choice solution [10], [11], [12]. The default underlying assumption for this simple relation is the absence of multiplicative noise, which is directly related to various kinds of low-frequency drifts in the system. Two important sources of such drifts are the LNA gain fluctuations and LFN components in the standalone detector circuits. Therefore, the LFN corner frequency sets another critical design aspect that is not always fully considered in the literature. Interesting to notice is that total-power radiometer chips with LNA preamplification implemented in SiGe HBT technologies were demonstrated to provide superior LFN corner frequencies of 100–200 Hz [13], [14], indicating the possibility of using a Dicke-free architecture. Here, with exception of [21], [59], the D-band currently sets the upper-frequency limit for video-rate, sub-Kelvin NETD single-chip solutions in silicon technologies [13], [14], [15], [16], [17], [18], [19], [20]; as presented in Table I. Even though, broadband standalone LNAs have been already presented [71], [72], this limit is mainly imposed by a combination of a degraded NF [73], [74], [75], [76], [77], [78], [79] and narrow radiometer system RF bandwidth.

Toward an upper-frequency limit of 1 THz or above, preamplification becomes unfeasible and NETD is solely related to the key figures-of-merit of a standalone detector, according to the

TABLE I
STATE-OF-THE-ART OF SILICON-INTEGRATED TOTAL POWER RADIOMETERS WITH LNA PREAMPLIFCATION ABOVE 110 GHZ

Techn.	B [GHz]	$R_{v,\max}$ MV/W	$NEP_{\min}$ [fW/$\sqrt{\text{Hz}}$]	LNA $G_{\max}$ [dB]	LNA $NF_{\min}$ [dB]	P_{DC} [mW]	τ_I [ms]	NETD [K]	Thermal Resp. [µV/K]	Dicke/ Antenna	Ref.
120 nm SiGe	95-135	6.4	7.1	29	6.1	25	30	0.12	-	Yes/No	[15]
130 nm SiGe	110-155	688	9.3	33	4.8	33.8	30	0.13	-	Yes/No	[16]
90 nm SiGe	∼132-142	52	1.4	36	7.9	47.2	3.125	0.25	4	No/No	[14]
65 nm CMOS	∼135-157	1.2	26	31	8.8	152	30	1.5	-	Yes/No	[17]
130 nm SiGe	∼160-170	28	14	≥35	8.24	95	3.125	0.25	8	No/No	[13]
130 nm SiGe	∼217-255	0.3	200	21	12	43	1000	0.5	0.04	No/Yes	[59]
130 nm SiGe	∼130-280	59	23	∼37	6.9	160	3.125	0.31	55	No/Yes	[21]

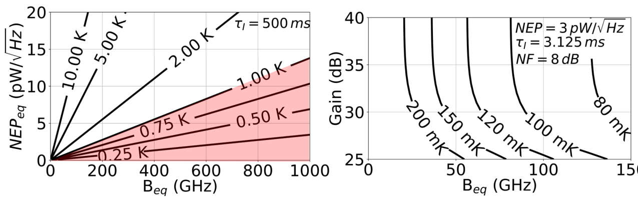

(a) (b)

Fig. 1. Theoretically achievable NETD for (a) the detector-first, and (b) LNA-first architecture as a function of the most relevant design parameters. For the preamplified implementation, a set of typical D-band circuit figure-of-merit values, according to Table I, was chosen for the calculation. In both cases, the impact of any multiplicative noise sources is omitted.

following:

$$NETD = \frac{NEP_{\text{eq}}}{\sqrt{2\tau_{\text{int}}}k_B B_{\text{eq}}} \tag{1}$$

where B_{eq} is a noise-equivalent RF bandwidth for the detector with a frequency-dependent responsivity, NEP_{eq} denotes the corresponding equivalent 1-Hz NEP (W/$\sqrt{\text{Hz}}$) in this bandwidth, and τ_{int} refers to the postprocessing integration time. Similarly to the preamplified total-power radiometer, (1) indirectly assumes no impact of detector low-frequency noise, which is only true in the far-out range of the detector noise floor. This time, however, the LFN corner-frequency for the majority of highly integrated solutions extends to substantially higher dc-offset frequencies, thus making the detector minimum-NETD operation a way more difficult to achieve with the practical imager implementations. Therefore, the low-frequency noise analysis and its experimental verification under the most relevant bias conditions should become one of key design aspects for each considered device technology. For LNA-first radiometers, a video-rate, sub-Kelvin NETD performance becomes feasible with narrowband operation [see Fig. 1(b)]. With reference to Table II, one should further notice that most of the best-in-class NEP values corresponding to a variety of highly integrated solutions were demonstrated across a narrow operation bandwidth which is insufficient to demonstrate NETD below 1 K with uncooled silicon-integrated THz direct detectors. Therefore, current passive imagers still rely on more sophisticated and integration-incompatible cooled implementations [6], [8], as indicated in Table II.

Further, a graphical representation of (1) shown in Fig. 1(a) demonstrates the theoretically achievable minimum detector NETD as a function of NEP_{eq} and B_{eq}. For a 0.5 K NETD imager operating with a refreshment rate as low as 1 Hz, an equivalent bandwidth of at least 150–200 GHz is required for an antenna-coupled direct detector with an optical NEP_{eq} of around 1 pW/$\sqrt{\text{Hz}}$. Such a low NEP_{eq} has not been reported so far for the room-temperature operated highly integrated detectors implemented in silicon and also in III-V technologies, as presented in Table II. Considering that state-of-the-art realistic NEP values are in a few pW/$\sqrt{\text{Hz}}$-range, the required RF bandwidth quickly extends to values exceeding 500 GHz. From this simple calculation, one can easily notice that the detector topology, its low-frequency noise behavior, an understanding of the detector static, and THz rectification and antenna co-design aspects become critical for a successful implementation of a passively operated imager.

III. CHOICE OF ANTENNA/DETECTOR TOPOLOGY

The choice of a suitable circuit topology with an accompanying antenna layout is the first and the most critical decision to be made for broadband operation of an antenna-coupled power detector. Considering that the currently foreseeable NEP values for silicon technologies are lower-limited to single-digit pW/$\sqrt{\text{Hz}}$ values, RF operation bandwidth of at least a few hundred GHz should be realistically considered to come close to a sub-Kelvin thermal resolution (NETD). At this point, it is important to emphasize that by operation bandwidth not only power matching, but also a suitable polarization-independent optical quality of radiation patterns is meant. From that point of view, a circularly-shaped compact antenna layout with rotational symmetry and two concentrically located orthogonal detection paths, as shown in Fig. 2 [34], is an ideal candidate. Such an arrangement, although compact, is very challenging from the antenna-circuit codesign point of view because the dual-path detector circuitry requires multiple dc signals to be wired down to the antenna center with minimum degradation of RF performance across sub-THz fractional bandwidth. By similar reasoning, any classical resonant-like matching style is initially ruled out due to the apparent space constraints but, more importantly, due to its unsuitability to synthesize a complex frequency-dependent impedance shaping the detector responsivity. Therefore, the chosen antenna topology should be inherently capable of providing a suitable impedance trajectory driving the detector input. More precisely, this impedance should ideally stay inductive across the entire operation bandwidth to counteract the capacitive nature of a bipolar transistor, as will be evidenced in the following sections.

The initial analysis of the detector circuit topology following below refers to an ideal case. All practical challenges related

TABLE II
STATE-OF-THE-ART OF THZ DETECTORS WITHOUT PREAMPLIFICATION

Detector type	Frequency Band 3dB|10dB [GHz]	Max. Responsivity	LFN corner	Min. NEP (@Freq) [pW/$\sqrt{\mathrm{Hz}}$]	Min. NETD [mK]	τ_{int} [ms]	Cooled	Ref.
SiGe HBT (130 nm)	**365–512 | 200–960 |$\mathbf{B_{eq}}$: 512**	**11.2 kV/W | 6.1 A/W**	**$\sim$ 1 kHz**	**2.3 (430 GHz)**	**860|640[†]**	**500**	**No**	**This work**
SiGe HBT (130 nm)	370–530 | 252–965 |$\mathrm{B_{eq}}$: 505	7 kV/W | 3.8 A/W	$\sim$ 20 kHz	2.7 (476 GHz)	–	–	No	[28], [51]
SiGe HBT (130 nm)	275–525 | 254–898 |$\mathrm{B_{eq}}$: 498	9 kV/W | 5 A/W	$\sim$ 20 kHz	1.9 (292 GHz)	–	–	No	[27], [28]
SiGe HBT (130 nm)	242–270* | 225–> 320*	2600 kV/W	$\sim$ 30 kHz*	7.9 (260 GHz)	–	–	No	[60]
SiGe HBT (130 nm)	285–347 | –	6.1 kV/W	–	21.2 (315 GHz)	–	–	No	[61]
SiGe HBT (180 nm)	308–333 | –	18 kV/W	$<$ 1 kHz	34 (320 GHz)	–	–	No	[62]
SiGe HBT (130 nm)	273–338 | 200–> 1000 |B_{eq} : 582	13 kV/W	$\sim$ 1 kHz	16 (1000 GHz)	–	–	No	[52]
SiGe HBT (250 nm)	650–850 | –	1 A/W	–	50 (700 GHz)	–	–	No	[50]
Microbolometer	100–1100	–	–	0.025	105	10	Yes	[8]
Microbolometer	100–1000	100 A/W	–	2	300–500	100	Yes	[9]
Bolometer (TES)	–	–	$\sim$ 10 Hz*	0.001	150	2	Yes	[23]
Bolometer (KID)	200–700	–	–	0.016	110–190	500	Yes	[6]
Bolometer (SOI CMOS)	600–1200 | –	600 mA/W	–	25	–	–	No	[63]
Bolometer (SOI CMOS)	$<$1500	2.1 A/W	$<$ 30 Hz	6.1	4700	172	No	[64]
NMOS (90 nm CMOS)	100–1500 (flat)	40 mA/W	–	42	4400	600	No	[65]
NMOS (65 nm CMOS)	790–960* | 680–>1100*	140 kV/W	–	100	20860	342000	No	[66] [36]
NMOS (65 nm CMOS)	290– 340 | -	2 kV/W	$\sim$ 10 Hz*	3.5 (315 GHz)	–	–	No	[29]
NMOS (90 nm CMOS)	605–630* | 570–670*	–	–	8 (620 GHz)	–	–	No	[67]
NMOS (90 nm CMOS)	356–367* | 328–387*	1.85 kV/W	–	40 (365 GHz)	–	–	No	[68]
NMOS (150 nm CMOS)	–	0.35 kV/W	–	42 (595 GHz)	–	–	No	[69]
NMOS (180nm CMOS)	–	5.5 kV/W	–	9.1 (650 GHz)	–	–	No	[39]
NMOS (65 nm CMOS)	650–825* | –	2.2 kV/W	–	14 (724 GHz)	–	–	No	[40]
NMOS (130 nm CMOS)	800–850 * | –	3.46 kV/W	4 MHz	12.6 (823 GHz)	–	–	No	[42]
NMOS (22 nm SOI CMOS)	700–1000 | –	1.51 kV/W	–	12 (855 GHz)	–	–	No	[41]
NMOS (65 nm CMOS)	850–1200 | 580–> 2200*	0.765 kV/W	10 Hz	25 (1011 GHz)	–	–	No	[70]
AlGaN/GaN-HEMT	700–900 (flat)	5.7 A/W	–	0.3/4.5	370/-	200/-	Yes/No	[30]
InP DGG-HEMT	–	2.2 kV/W	–	15 (1000 GHz)	–	–	No	[31]
SBD (22 nm CMOS)	200–280 | 200–> 600*	25 kV/W	4 MHz	20 (200 GHz)	8000*	1000	No	[32]
SBD (130 nm CMOS)	273– 286 * | -	0.336 kV/W	4 MHz	29 (280 GHz)	–	–	No	[48]
P-N Diode (45 nm CMOS)	–	0.558 kV/W	1 kHz	56 (780 GHz)	–	–	No	[47]
N-FinFET (16 nm FinFET)	580–590 * | 530–600 *	88.8 kV/W	$\sim$ 200 Hz*	8.7 (554 GHz)	–	–	No	[43]

[†] Single/Dual pol. * Calculated from graph.

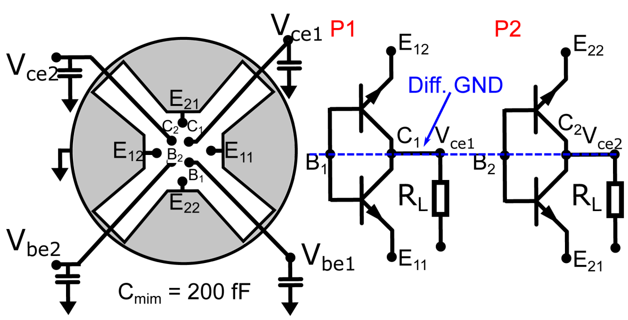

Fig. 2. Simplified schematic of a dual-path detector co-integrated with a polarization-diversity on-chip antenna. Two orthogonal polarization paths, named P1 and P2, do not share any dc supply networks to improve the inter-path isolation. An AC ground (Diff. GND) is only valid for all odd harmonics of the fundamental RF frequency.

to implementing such a detector at THz frequencies will be addressed in the following sections. The main focus will be given to the antenna-circuit codesign aspects as the analysis of the standalone antenna was already covered in our previous publications [28], [34], [51].

A differentially operated minimum-size device pair ($A_e = 0.96 \times 0.1\ \mu\mathrm{m}^2$) in common-base (CB) topology was chosen for detector implementation. This choice is driven by multiple reasons. The minimum device size optimizes the detector performance at THz frequencies [28], whereas device operation in CB configuration promises the highest matching potential in terms of bandwidth and Q-factor [50], provided that a broadband dc return path at the emitter nodes can be effectively established. This, combined with the differential operation, results in the following important advantages in terms of detector layout and operation bandwidth. First of all, a set of ac grounds (Diff. GND in Fig. 2) is established between the relevant external base and collector nodes for the fundamental RF frequency and its all odd harmonics. This initially confines the detector RF operation to two miniature-size b-e diodes, minimizing the impact of parasitic feedback paths between base and collector nodes as well as large collector-to-substrate subnetworks with low-modeling accuracy. Considering further that detector is operated with low input power levels, even harmonics leaking at the base and collector nodes are not sufficiently strong to deteriorate the detector responsivity. Noting also that common-mode signaling refers to a common ground, the even harmonic currents can be further attenuated with a purely differential layout of the detector circuitry as well as the antenna, making its performance largely independent from the high-frequency terminations at the base and collector nodes.

IV. LOW-FREQUENCY ASPECTS OF DETECTOR OPERATION

For a proper understanding of detector rectification fundamentals, a nonlinear device model of the CB detector circuit from Fig. 2 is presented in Fig. 3. With this model differences in between different device bias regions are investigated in the following indicating tradeoffs in power consumption and device performance towards a future large scale FPA design.

A. Nonlinear Equivalent Detector Model Parameters

The equivalent model parameters were extracted from the fab-supported fully numerical HiCUM device model [80]. The presence of a virtual ac ground at the external base and collector nodes (Diff. GND) is only valid for all odd harmonics of the fundamental RF frequency but fully justified for the following simplified analysis as the second-order high-frequency currents are very low for the normal detector operating conditions. The equivalent components marked in red are essential for device

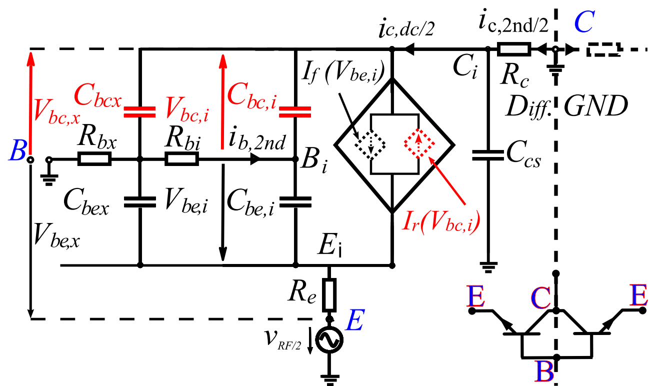

Fig. 3. Nonlinear equivalent model of a single device in the detector configuration with a topology-enforced ac ground, (Diff. GND), at the external base and collector nodes valid for all odd harmonics of the fundamental RF frequency. The model parameters marked in red become important for the device operating in saturation.

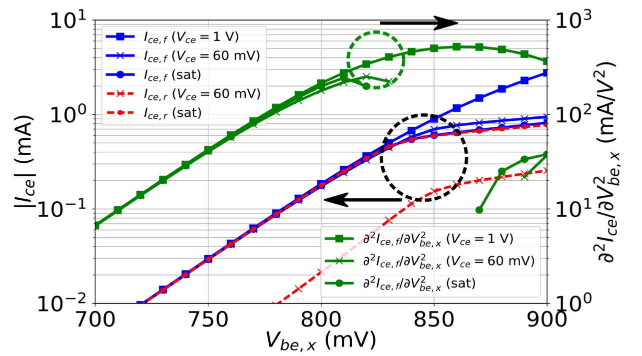

Fig. 4. Simulated evolution of the voltage-controlled current sources I_f and I_r from Fig. 3 as a function of the external base-emitter voltage, $V_{\text{be},x}$. The second-order derivatives of I_f with respect to $V_{\text{be},x}$ for different device bias regions are also plotted. Contrary to the device in saturation, $V_{\text{be},i}$ and $V_{\text{be},x}$ differ substantially for the forward-active operation at high injection currents due to the large emitter resistance, R_e.

TABLE III
ACCESS RESISTANCE VALUES FOR THE MINIMUM-SIZE DEVICE

R_{bi}	R_{bx}	R_e	R_c
72 Ω	26 Ω	14 Ω	26 Ω

operation in saturation, corresponding to a b-c diode's forward bias. For initial low-frequency analysis, all high-frequency effects related to the presence of multiple internal "RC" time constants can be ignored. The key components defining the detector operation near dc are two nonlinear voltage-controlled current sources, $I_f(V_{\text{be},i}, V_{\text{bc},i})$ and $I_r(V_{\text{bc},i})$, that correspond to the forward- and reverse-active device operation range, respectively, and a set of device contact resistances with the corresponding values gathered in Table III. For low-to-medium injection currents, all contact resistances are nearly constant. The base resistance is split into two parts referring to the internal and external device regions, which is important for proper high-frequency modeling.

It is important to notice that I_f, the primary source of detector rectification, is not only a function of internal b-e voltage, $V_{\text{be},i}$, but also depends on $V_{\text{bc},i}$. As evidenced in Fig. 4, this dependence is strong for a sufficiently large charge injection into the internal base region from the collector node, which occurs for an appropriately low collector voltage V_{ce}. To investigate its influence on the detector rectification potential as well as to include the linearizing impact of a series-feedback contact resistance, R_e, the second-order derivatives of I_f with respect to the external b-e dc voltage, $V_{\text{be},x}$, were calculated and are gathered in Fig. 4. For the device in the forward-active region, the rectification potential of a standalone current source, I_f, is maximized before the onset of high-current effects and occurs for $V_{\text{be},x}$ of around 850 mV in the technology node under investigation. Considering further that in this operation range, the far-out noise floor is dominated by shot noise with its square-root dependence on dc current, the following simple metric $\partial^2 I_f/\partial V_{\text{be},x}^2/\sqrt{I_f}$ can be introduced to search for the optimum NEP bias point at low frequencies while driven from an ideal ac voltage source. This metric indicates a downshift of the optimum $V_{\text{be},x}$ by around 30 mV toward 820 mV, setting an initial comparison base for other device operation ranges. Here, it becomes evident from Fig. 4 that $\partial^2 I_f/\partial V_{\text{be},x}^2$ for both weak as well as deep device saturation does not degrade considerably with $V_{\text{be},x}$ of up to around 800–810 mV but the corresponding noise analysis becomes more involved and will be addressed in the following section. Finally, with reference to [28], a total rectified dc collector current can be approximated with the following simplified (2), which includes multiple high-frequency effects being the subject of a more detailed analysis in the following sections. At the moment, only the first three components become relevant for low-frequency analysis. In particular, the terms I and II present an alternative form of the previous analysis with all partial derivatives referring to $V_{\text{be},i}$ and $G_{m,f}$ defined by $\partial I_f/\partial V_{\text{be},i}$, which corresponds to a classical transistor transconductance. The entry III, representing an ac transfer function between $v_{\text{be},i}$ and $v_{\text{be},x}$, needs to be evaluated near dc, resulting in a strong $1/(1 + G_{m,f} \cdot R_e)^2$ responsivity scaling factor as compared to an ideal detector with zero-Ω emitter contact resistance.

$$|i_{c,dc}| = |\underbrace{\boxed{\frac{\partial^2 I_f}{\partial V_{\text{be},i}^2}}}_{\text{I}} \cdot \underbrace{\boxed{\frac{1}{1 + G_{m,f} \cdot R_e}}}_{\text{II}} \cdot \underbrace{\boxed{\left(\frac{(Z_{Cbe} + R_b)||\frac{1}{G_{m,f}}}{(Z_{Cbe} + R_b)||\frac{1}{G_{m,f}} + R_e} \cdot \frac{Z_{Cbe}}{Z_{Cbe} + R_b}\right)^2}}_{\text{III}} \cdot \underbrace{\boxed{P_{Ant} \cdot Re\{Z_{Ant}\} \cdot \left(\frac{Z_{Det}}{Z_{Ant} + Z_{Det}}\right)^2}}_{\text{IV}}| \quad (2)$$

B. Detector Readout and Bias Scheme

Concerning Figs. 2 and 3, the rectified dc output current, according to (2), incurs a voltage drop across the detector output resistance, Z_{Out}, defining a final output signal to be processed by the subsequent low-noise readout chain. Although the relation

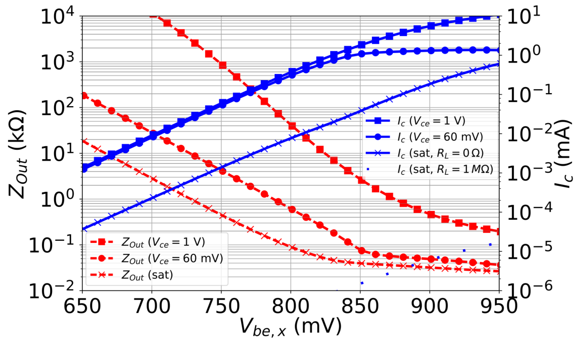

Fig. 5. Simulated detector bias current, I_c, with the corresponding output impedance for different bias regions as a function of $V_{\mathrm{be},x}$. The bias region is set by a dc collector voltage, V_{ce}. It corresponds to forward-active operation for 1 V and to weak saturation for 60 mV. For deep saturation, two distinct operation conditions are defined with R_L of 0 Ω and 1 MΩ. In the former, the detector output is short-circuited with an ideal 0 V voltage source, whereas the latter corresponds to the collector node left unbiased.

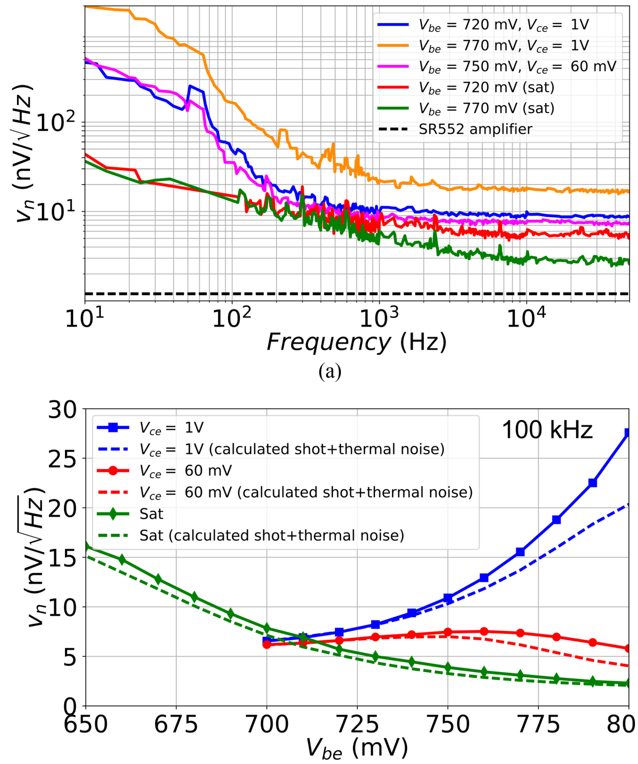

(b)

Fig. 6. Detector noise characteristics. (a) Measured spectral density of the detector output noise voltage for some selected representative bias points corresponding to forward-active, weak saturation, and deep saturation region. (b) Simulated and measured detector noise floor at 100 kHz dc frequency offset as a function of V_{be}.

between the detector current (R_i) and voltage responsivity (R_v) in the forward-active range is set by the external load resistance R_L as $R_v{=}R_i\cdot R_L$, the situation gets more complicated at a sufficiently low collector bias voltage, in particular for $V_{\mathrm{ce}}{=}0$ V. In this case, Z_{Out} is established by a parallel connection of R_L and $1/G_{m,r}$, where $G_{m,r}{=}\partial I_r/\partial V_{\mathrm{bc},i}$ is an equivalent dynamic conductance of both b-c diodes near dc with indirect nonlinear dependence on $V_{\mathrm{be},x}$ for a fixed collector voltage, V_{ce}. In the limiting case, the output collector nodes can be left unbiased, resulting in the detector cold operation with a near-zero bias current. The simulated detector output impedance with the corresponding bias current I_c plotted in Fig. 5 as a function of $V_{\mathrm{be},x}$ for different bias regions. As can be noticed, Z_{out} in saturation (sat, $R_L = 0\,\Omega$, $V_{\mathrm{ce}} = 0$ mV) drops very quickly with an increase of $V_{\mathrm{be},x}$ reaching near 100 Ω at around 800 mV, and, thus, makes it virtually impossible to establish a current-mode readout scheme. Simultaneously, a very low dc current largely eliminates shot noise from the succeeding noise analysis.

To facilitate the performance comparison between different detector bias regions, a voltage readout scheme with voltage responsivity, R_v, was chosen. For operation in the forward-active range as well as in weak saturation ($V_{\mathrm{ce}} = 60$ mV), the detector output impedance is established with an external load resistance, R_L, whereas for cold operation ($V_{\mathrm{ce}} = 0$ mV) the device collector nodes are left unbiased and connected directly to the input of a low-noise amplifier. Contrary to the forward-biased device with straightforward relation $R_v{=}R_i\cdot R_L$, the corresponding R_v dependence on $V_{\mathrm{be},x}$ with the fixed collector voltage, V_{ce}, becomes a nontrivial function due to different doping profiles of the b-e and b-c diodes. In particular, as discussed in [28], the detector R_v peaks at low V_{be} bias voltages that do not correspond to the minimum NEP operation, even though the detector current responsivity, R_i, indicates a bias-range insensitive dependence on $V_{\mathrm{be},x}$ up to high-current injections.

C. Detector Noise

To minimize the detector noise, special attention needs to be paid to the choice of R_L as well as the source resistance of the dc voltage supply networks. Initially, the far-out noise spectrum is only considered as it sets the lower limit of the detector output noise floor. To minimize the influence of thermal noise related to the load resistance, R_L, on the detector NEP, its value needs to be maximized. For low detector power dissipation, R_L of 1.8 kΩ was chosen with minimum noise penalty as compared to the equivalent current-mode readout. With respect to the bias system, the base nodes are critical. They are a source of the shot noise current with the corresponding noise voltage across the external base resistance, which appears at the output with some multiplication factor. This factor is defined by a suitable noise transfer function related to the transistor static current gain, β, near dc, and therefore varies across the device bias range [28]. More specifically, the operation in deep saturation indicates practically zero sensitivity to the external base resistance. In contrast, this resistance needs to stay appropriately low for the device in the forward-active range. In particular, it should be kept below around 500 Ω for the minimum-size device in the chosen technology node. The simulated as well as the measured detector far-out noise voltage spectral density (@ 100 kHz dc-offset) is presented in Fig. 6(b) for different device bias regimes. Easily to notice are the opposite noise evolution trends for the forward-active and the cold operation as a function of $V_{\mathrm{be},x}$, which is directly related to the bias-dependent Z_{Out} of the saturated transistors. An interesting behavior can be observed for V_{ce} around 60 mV with only weak noise voltage dependence on $V_{\mathrm{be},x}$, where an increase in the noise current is balanced by the corresponding decrease of Z_{Out}.

Apart from the thermal and shot noise components dominating the device far-out noise, the other LFN components such as $1/f$ and G-R (generation-recombination), are typically deficient in terms of the modeling accuracy which in turn requires substantial effort in experimental characterization. Particularly challenging are the miniature-size devices operating at low bias currents. Noise modeling for HBT devices in saturation is practically missing [28], [81], [82], [83], [84], [85]. A selected set of the measured LFN spectra for different detector bias conditions is shown in Fig. 6(a). The chosen base voltages represent the detector bias range where the near-optimum NEP operation is expected. The detector was supplied from a battery-operated low-noise and low-impedance power supply unit to minimize the number and intensity of possible spurs in the measurement setup. The detector biased in the forward-active range @ 770 mV shows a near ideal $1/f$ slope for dc-offset frequencies of around 100–1000 Hz, which is directly related to the nonnegligible collector dc current. Qualitatively similar behavior, although with a degraded slope, can still be observed for lower V_{be} values provided the device is operated at least in weak saturation with a decent amount of dc current. The noise characteristics in the 10–100 Hz range can be attributed to the presence of G-R time constants [86]. Interesting to notice is that for cold-operated devices, the regular $1/f$ slope disappears from the LFN spectrum but the G-R related components are still present. Another relevant observation is that the far-out noise floor is achieved at higher dc-offset frequencies as compared to the corresponding noise characteristics in the forward active range, although the overall noise floor gets lower and a distinct $1/f$ corner frequency cannot be identified. It directly results from the missing shot noise in the measured spectrum. Unfortunately, the frequency upshift of LFN may unexpectedly have negative consequences for practical detector operation scenarios with the necessity of more frequent calibration. The flattest frequency roll-off of the noise spectrum is demonstrated where the G-R determined LFN intersects with an increased thermal noise of the cold device biased @ 720 mV. As will be shown later, this operation point, however, does not correspond to the minimum detector NEP at THz frequencies.

V. Detector Rectification at THz Frequencies

In order to investigate the major degradation mechanisms of the detector current responsivity, R_i, at THz frequencies, first the inherent device rectification properties should be studied without the influence of the detector-antenna matching network which can be done assuming an ideal 0 Ω RF voltage source drive. Under this condition, the most important function limiting the internal detector voltage drive and as such its rectification potential is the ac-transfer function between the external and internal device nodes according to Fig. 3.

A. AC Transfer Function of External to Internal Detector Nodes

The external to internal detector node ac transfer function is defined by the third term of (2) which should be first studied in

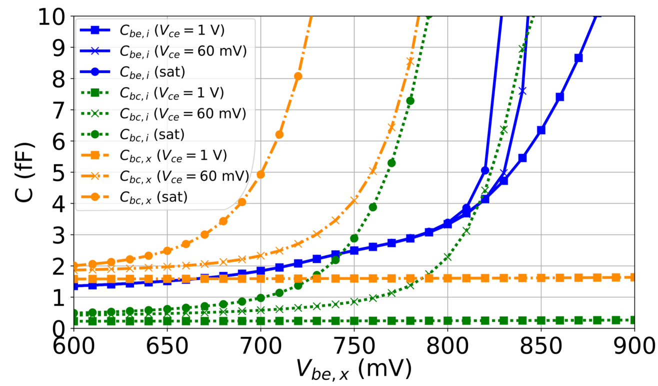

Fig. 7. Evolution of the major device capacitances as a function of $V_{\mathrm{be},x}$ for three selected bias regions denoted by different V_{ce} values.

combination with the relevant model details from Fig. 3. Term III represents the aggregate impact of two main low-pass time constants created by $R_{b,i(x)}$, R_e, and $C_{\mathrm{be},i(x)}$ on the frequency-dependent degradation of $v_{\mathrm{be},i}$ at the fundamental RF frequency, while the parasitic device components between base and collector nodes are still ignored. As previously shown in Table III, the major access resistances for the minimum-size device are nonnegligible and, therefore, their impact on detector operation can be expected to be significant. In particular, the ideal initial assumption of a zero-voltage swing between the internal "b" and "c" nodes is completely violated, which has main implications for the detector operating in saturation. For quantitative analysis of the time constants, a bias dependence of the major internal capacitances is additionally plotted in Fig. 7. Similarly to I_f, the internal base-emitter capacitance, $C_{\mathrm{be},i}$, strongly relates to the collector voltage, V_{ce}, at sufficiently high injection currents. However, for base-emitter voltage, $V_{\mathrm{be},x}$, below 800 mV, where minimum-NEP operation is expected, the differences in $C_{\mathrm{be},i}$ for all operation ranges are insignificant, thus, making the term III in (2) as well as the detector input impedance vastly insensitive to the detector bias regime. The first significant drop in the frequency-dependent detector current responsivity R_i is mainly attributed to the base contact resistance, $R_{b,i}$+$R_{b,x}$, and occurs around 500–600 GHz for the optimum detector bias conditions. The impact of the time constant $R_e \cdot C_{\mathrm{be}}$ becomes first noticeable at around 1 THz. The feedback path between the detector input and output ports provided by the capacitance, C_{bc}, divided into an external and an internal component, $C_{\mathrm{bc},x}$ and $C_{\mathrm{bc},i}$, respectively, is activated at THz frequencies due to the presence of contact resistances R_b and R_c. However, contrary to the device operating in the common emitter configuration, its impact on the responsivity R_i and the corresponding input impedance Z_{Det} of the forward-active biased detector is insignificant as it is largely bypassed by the dominant low-pass behavior of R_b and C_{be}. A bias-dependence of $C_{\mathrm{bc},x}$ and $C_{\mathrm{bc},i}$ is plotted in Fig. 7 for completeness. A remarkable difference in the capacitance values between the saturation and the forward-active range is straightforward to notice. However, apart from some differences in Z_{Det}, it has no direct negative consequences on R_i of the detector in saturation. Here, more important is the leakage of the fundamental driving voltage, $v_{\mathrm{be},i}$, to $v_{\mathrm{bc},i}$ of the

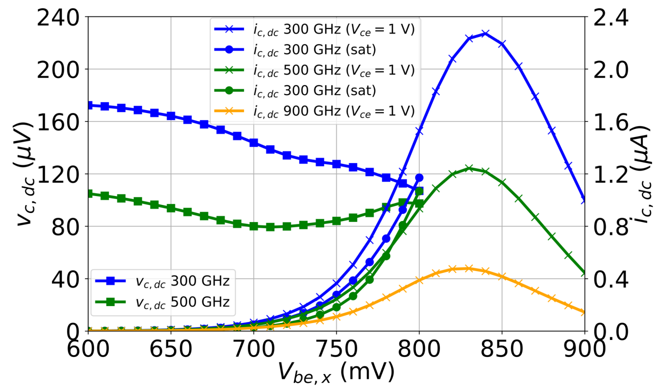

Fig. 8. Simulated rectified dc output current, $i_{c,dc}$, while driven by an ideal 10 mV RF voltage source for some selected operation frequencies. For the detector in saturation, an additional voltage response, $v_{c,dc}$, is also plotted.

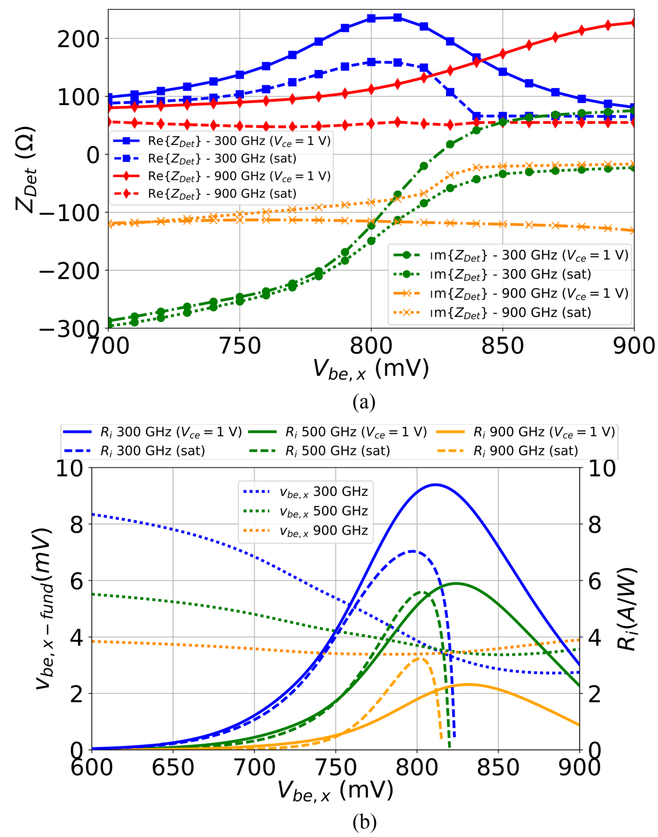

Fig. 9. (a) Simulated input impedance, Z_{Det}, at 300 GHz and 900 GHz as a function of $V_{\mathrm{be},x}$, for the detector biased in the forward-active range as well as in saturation. (b) The corresponding RF driving voltage, $v_{\mathrm{be},x}$, and the current responsivity, R_i, of the conjugately matched detector.

forward-biased b-c diode due to the missing virtual ac ground between the collector and base nodes. This leakage is incurred by a low-impedance of $C_{\mathrm{be},i}$, which shunts the b-e diode. The fundamental RF voltage $v_{\mathrm{bc},i}$ grows quickly with an increase of the bias voltage V_{be} and can be as high as $v_{\mathrm{be},i}$ around 1 THz. Note that $v_{\mathrm{bc},i}$ drives the current source I_r (see Fig. 3), which is a source of parasitic out-of-phase rectification for the forward biased b-c diode. This phenomenon is the most important extra factor of the responsivity degradation at the higher-end of operation bandwidth compared to the forward-active operation. For an unfavorable combination of the bias voltages V_b and V_c, the detector response can potentially decrease to zero at frequencies around 1 THz or higher.

For the final comparison between different detection bias regions, Fig. 8 presents the simulated rectified detector output current, $i_{c,dc}$, for three chosen RF frequencies as a function of $V_{\mathrm{be},x}$ while driven by an ideal zero-Ω 10 mV RF voltage source. It can be noticed that differences in the current values for both regions of operation do not significantly deviate from each other for the base bias voltage of up to 800 mV, as expected from the previous analysis. For higher $V_{\mathrm{be},x}$, the simulations experience some convergence issues resulting in nonphysical values that cannot be verified by measurements. As this issue accelerates with frequency, we attribute this to deficient modeling accuracy of C_{bc}, I_f, and I_r for higher current injections. For completeness, the complementary voltage response, $v_{c,dc}$, of the detector in saturation is additionally plotted. In this case, the response further includes the impact of the bias-dependent dynamic output conductance, $G_{m,r}$, as shown in Fig. 5. The voltage response is maximized at low bias points which, in view of the noise analysis from Fig. 6, does not correspond to the minimum-NEP operation. As shown later, a low NEP is achieved for bias points corresponding to a higher current responsivity R_i, independently from the bias operation range. It is further interesting to notice that R_i peaks at lower $V_{\mathrm{be},x}$ values as compared to those previously predicted from low-frequency analysis (see Fig. 4) to counteract the frequency roll-off of $v_{\mathrm{be},i}$ according to the third term in (2).

B. RF Power Transfer Between Antenna and Detector

All previous analyses referred to an ideal 0 Ω RF voltage source which becomes unavailable in RF domain. Under real driving conditions, THz power is provided from a complex-impedance antenna and the fundamental driving voltage, $v_{\mathrm{be},x}$, results from the interplay of the detector and antenna impedances, Z_{Det} and Z_{Ant}. This is represented by term IV in (2). As the rectified RF current quadratically depends on $v_{\mathrm{be},x}$, the simple assumption of a conjugate match does not guarantee the maximum response. A careful inspection of term IV leads to the conclusion that the RF driving voltage is maximized not only for large magnitudes of Z_{Det} and Z_{Ant} but more important where both impedances become predominantly reactive, thus, staying contrary to the classical design style and challenging the effectively achievable RF operation bandwidth. To facilitate further analysis, the simulated bias-dependence of Z_{Ant} for two selected RF frequencies and two distinct bias operation regions are presented in Fig. 9(a). As pointed out by the previous analysis, Z_{Det}, in particular its imaginary part, for both operation ranges and the base bias voltage corresponding to the expected detector optimum performance ($V_{\mathrm{be},x} \leq 800$ mV) are reasonably comparable. The major difference appears in $Re\{Z_{\mathrm{Ant}}\}$ and results from the large C_{bc} values in saturation

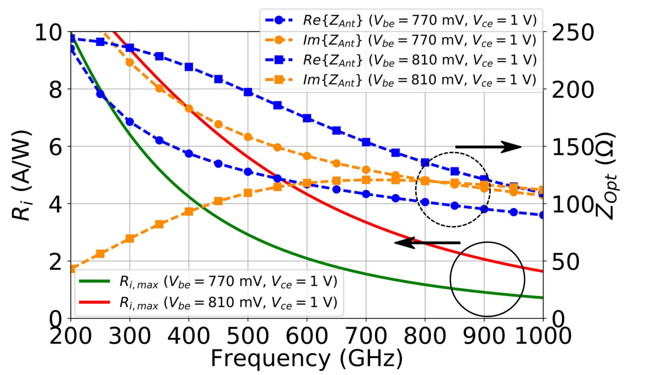

Fig. 10. Simulated frequency-dependent current responsivity, R_i, with the corresponding optimum antenna driving impedance, $Z_{\rm Opt}=Z^*_{\rm Det}$, for two selected $V_{{\rm be},x}$ values of 810 mV and 770 mV, which result in maximum R_i and minimum NEP, respectively, at 300 GHz.

short-circuiting the largest contact resistance $R_{b,i}$ but with rather insignificant impact on detector rectification; provided the b-c diode is reverse-biased. As the trends representing the $Z_{\rm Det}$– and R_i–dependence on $V_{{\rm be},x}$ are, in general, different, the maximum driving RF voltage and the maximum R_i are not simultaneously achieved, thus resulting in a frequency-dependent new optimum location of the bias point trading both factors. This behavior is shown in Fig. 9(b) for some selected frequencies. By comparison to the previous analysis with an ideal RF voltage source, the optimum bias point moves again toward lower $V_{{\rm be},x}$ values around 800 mV, where the fundamental RF driving voltage, $v_{{\rm be},x}$, grows thanks to an increase of $Im\{Z_{\rm Ant}\}$. This phenomenon is more pronounced in the lower frequency end due to still sufficiently large impedance levels associated with the relevant internal device capacitances. For analogous reasons, the optimum $V_{{\rm be},x}$ around 1 THz moves to higher values where $v_{{\rm be},x}$ already shows a weak dependence on the base bias voltage and where R_i can be simultaneously maximized. Similarly to Fig. 8, the simulation results for the detector in saturation exhibit some numerical issues at higher bias points, leading to nonphysical current response values exceeding those in the forward-active region of operation. The simulated frequency-dependent current responsivity, R_i, of the optimally-driven detector with the corresponding antenna driving impedances for two different bias points referring to the maximum response and the minimum NEP at 300 GHz are gathered in Fig. 10. The optimum antenna driving impedance shows a strong frequency dependence with the comparable real and imaginary parts. The requested Q-factor of $Z_{\rm Ant}$ can be partly reduced at lower frequencies with an increase of $V_{{\rm be},x}$, which is solely attributed to the device operating in CB topology, but at the cost of a substantial increase of $Re\{Z_{\rm Ant}\}$.

With reference to the same figure, the responsivity drops by around one order of magnitude across 200–1000 GHz, indicating the challenges related to a broadband low-NEP operation for passive imaging. Taking into account the previous noise analysis with the results from Fig. 6, the expected minimum NEP increases from around 1.2 $\text{pW}/\sqrt{\text{Hz}}$ at 300 GHz to 10.5 $\text{pW}/\sqrt{\text{Hz}}$ at 1 THz, not considering any antenna loss.

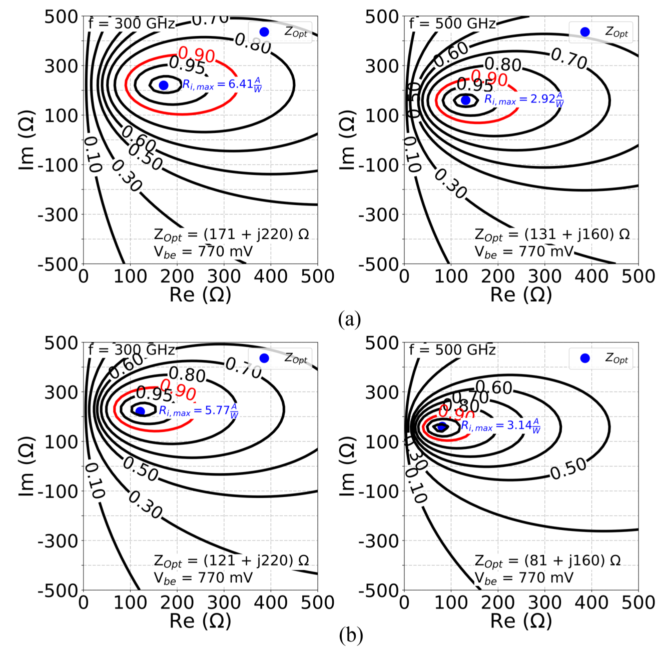

Fig. 11. Normalized contour plots of the detector current responsivity, R_i, as a function of the antenna impedance ($Z_{\rm Ant}$) at 300 GHz and 500 GHz for two operating regions: (a) forward-active, (b) saturation.

C. Detector Responsivity Contour Analysis

As frequency-dependent antenna impedance trajectories are not easy to synthesize with a small form-factor and minimum implementation loss, the sensitivity of the detector responsivity R_i to the antenna impedance deviations from the optimum trajectory are additionally investigated in the following. Some relevant exemplary results at two selected RF frequencies are given in Fig. 11 as 2-D contour plots. The contours show the relative drop of R_i as a function of $Z_{\rm Ant}$ with the detector biased @ 770 mV and operated in two distinct bias regions. Such contours can be used as a guideline to synthesize the suitable antenna geometry with a frequency-dependent impedance profile, resulting in a relatively constant distribution of R_i across the highest possible frequency range. Considering the higher R_i values toward lower RF frequencies, substantially larger impedance search space can be here used to achieve the design goals. Another important observation is that the higher $Z_{\rm Det}$ potentially provides a better design robustness because the contours of constant responsivity are less crowded than for lower impedance values. Unfortunately, broadband high-impedance antennas at THz frequencies are challenging to design and control in the presence of the surrounding layout circuitry. In line with the previous analysis, similar contour shapes are obtained for saturation and forward-active operation.

VI. Antenna Detector Codesign Aspects

The antenna design relies on the topology introduced in [34] and [51], but it includes multiple changes in its layout to address the mentioned codesign issues and to accommodate higher operation bandwidth in a similarly compact layout. The main antenna

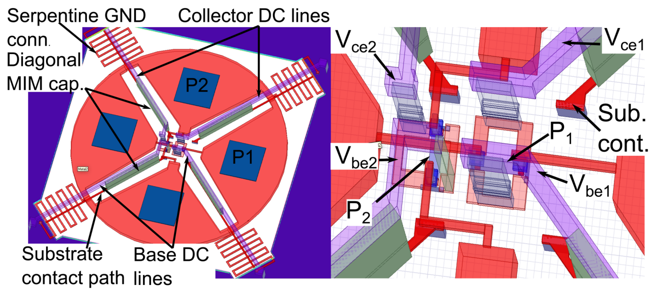

Fig. 12. Simulation model of the complete detector/antenna geometry. The common-base transistor circuits are placed at the antenna center. The right figure shows a detailed layout view down to the transistor level.

geometry was dimensioned to reach a low-NEP operation across at least a few hundred GHz toward passive imaging, considering the analysis results from the previous section. With the focus set on the complete antenna-coupled detector performance analysis, a detailed study investigating the tradeoffs in antenna efficiency and impedance trends based on the geometrical antenna shape is not covered by the manuscript. More details can be found in our previous publications [34], [41], [51], [87], [88]. For completeness, only the most general antenna features are outlined.

A. Leakage/Isolation Issues Related to Two-Path Operation

The simplified antenna-detector schematic from Fig. 2 does not reflect the practical implementation challenges related to a dual-channel detector operation that have been initially brought to attention in Section III. The key problem is related to the necessity of accommodating multiple devices near the antenna center and providing them with separate dc points without breaking the inherent circuit symmetries that guarantee dc-to-RF isolation and low leakage between both polarization chains. With a single linearly-polarized differentially-operated detection path, all necessary dc wiring can be laid out along the antenna H-plane, which in this case aligns with the physical location of the circuit-level ac ground at RF frequency, thus preserving all major features of the broadband detector configuration. With two orthogonal polarizations, this option becomes unavailable, which enforces a careful layout-oriented analysis of the entire pixel and is briefly covered in this section.

The antenna is buried in a thin seven-metal layer silicon dioxide BEOL stack, as shown in detail in [89], and illuminates a hyper-hemispherical silicon lens through the backside of a lossy 150 μm thick silicon substrate (50 Ω.cm). Its layout, shown in Fig. 12, includes two orthogonally oriented polarization paths, P1 and P2, with the corresponding differential RF ports around the antenna center, driving two pairs of devices from the emitter nodes. To minimize the chance of launching the parasitic common-mode currents and to keep operation bandwidth as well as radiation efficiency at maximum, the reference global ground is provided only outside of each detector pixel with a pixel pitch of 160 μm. To accommodate two device pairs, the center feed points for each polarization need to be offset from each other (zoom-in part of Fig. 12), thus breaking an ideal odd symmetry in each path as well as perfect orthogonality between both paths, not mentioning the differences in electrical lengths of the center feed lines. The latter results in differences in the antenna driving impedances growing with frequency increase. This was minimized with a suitable set of layout modifications in the antenna center along two paths. More important, the lack of perfect symmetry leads to an unavoidable leakage between both polarizations and between different transistor nodes of the same detection path. Particular attention should be paid to RF leakage to the forward-biased b-c junctions, which is a source of parasitic rectification for the detector in saturation. This calls for an accurate layout analysis and numerical optimization including the full device-level complexity.

B. Broadband DC Ground Path to the Emitter Nodes

Despite its broadband matching potential, the differentially-driven detector circuit in common-base configuration is challenging to implement if a near one-THz RF bandwidth is requested. This challenge is related to providing the dc return path to the transistor emitter nodes with minimum impact on its RF operation. For obvious reasons, this task can only be accomplished using the antenna layout without an additional dc-bias choke. For a single linearly-polarized differentially-operated antenna [27], the apparent solution is provided by its H-plane. This location becomes, however, unavailable due to the presence of another orthogonal polarization, making the entire detector design rather complicated. With the aid of EM field analysis, it was found that four diagonal locations of the main antenna ring can potentially provide low perturbation of the antenna RF functionality at higher operation frequencies thanks to an appropriate mode field confinement along two center feeds [34]. This option fails, however, in the lower frequency end due to the large spatial extension of E-fields along the ring perimeter. Therefore, simple grounding with straight transmission lines, sufficiently short to fit into the compact pixel pitch, will malfunction the antenna in the broadband sense. Four suitably sized symmetric serpentine-like grounding strips are accommodated within the compact antenna footprint to circumvent this limitation. For a proper understanding of the functionality provided by such grounding paths to the antenna ring at diagonal locations, the antenna differential operation needs to be first noticed. Under such driving conditions, the ground aperture surrounding the ring is excited differentially by two pairs of serpentines aligned along two corresponding diagonals. With a suitable ground aperture size and a sufficient length of the folded strips exceeding a quarter wavelength at the minimum operation frequency, a resonance-free impedance trajectory asymptotically increasing with frequency can be established along two diagonals at the connection points with the ring. The absolute impedance values can be made sufficiently high to minimize the ring loading effects by the serpentines to provide a broadband dc path to the device emitter nodes.

C. DC Bias Paths to the Base and Collector Nodes

Apart from providing a suitable level of RF driving impedances and dc ground return paths to the emitter nodes, multiple additional dc signals need to be routed to the detector center through the complete antenna layout with minimum degradation of the inherent detector performance, in particular its operation bandwidth.

First, for a proper operation of the collector-substrate subnetwork, the reference ground potential should be provided to the device proximity using the vertical substrate contacts. Because the global common ground is removed from the antenna layout, this task is accomplished with four low-level diagonal lines connected to the surrounding global ground around the pixel periphery (see Fig. 12). The lines are physically disconnected from the ground ring to minimize the impact of the line parasitic resonance effects on the antenna operation. They further provide a second-harmonic ground return path for four additional diagonal lines connecting each polarization path's base and collector nodes separately to the external dc voltage supply. A vertical space between the corresponding dc lines on the uppermost metal layer and the underlying ground strips is filled with a MIM cap layer to limit the RF electrical extension of the detector circuit at the base and collector nodes. According to full-wave EM simulations, this solution provides a 30–40 dB suppression of RF signals across 200–1000 GHz at the external dc supply ports around the pixel periphery. Due to the limited space in the crowded detector layout around the antenna center, the distributed MIM capacitance cannot be brought directly to the internal device nodes, thus, making it impossible to achieve a perfect ac short as in the detector schematic from Figs. 2 and 3. Here, the second-harmonic currents can be directly impacted, as well as the incoming fundamental signals in the absence of a perfect layout symmetry and due to the parasitic EM coupling between the main antenna geometry and the corresponding diagonal lines. A finite connecting distance of around 25 μm (including 12 μm of vertical space) between the grounded MIM capacitance and the corresponding base/collector node creates a nonzero load impedance which can be modeled with a frequency-dependent inductance ranging from around 16 pH to 30 pH across 200 to 1000 GHz.

To minimize the level of some parasitic leakages originating from EM coupling between different layout parts, all four diagonal lines needed to be assigned appropriately to the corresponding base and collector nodes, considering the presence of multiple symmetry planes and electrical path differences in the antenna layout. In particular, with respect to Fig. 12, the base and collector nodes for P1 are supplied from two dc lines on the right, whereas P2 is connected to two lines on the left. The main idea behind such an arrangement can be understood by considering P1 as an example. Each half of the differentially excited antenna results in distributed in-phase coupling to the corresponding top and bottom diagonal strips. Noting that both strips are connected to the base and collector nodes, this should ideally lead to a low RF fundamental leakage between the b-e and b-c diodes.

D. Complete Antenna/Circuit Layout

A complete, down-to-the-transistor level, multiport layout model was built and used in the optimization process with full-wave EM simulations to investigate the influence of the parasitic phenomena on the broadband operation of the dual-polarization detector. According to the simulation results, the most critical direct leakage between two RF ports at the emitter nodes corresponding to both detection paths is kept below –35 dB, independently from the detector RF termination impedances. The other parasitic coupling factors to the base/collector nodes depend on the device bias operation range (forward-active vs. saturation) and strongly vary across frequency. They are generally 1-to-2 orders of magnitude higher than the direct P1-to-P2 leakage, with the highest values near the lower end of RF bandwidth where the folded diagonal lines start loading the antenna ring.

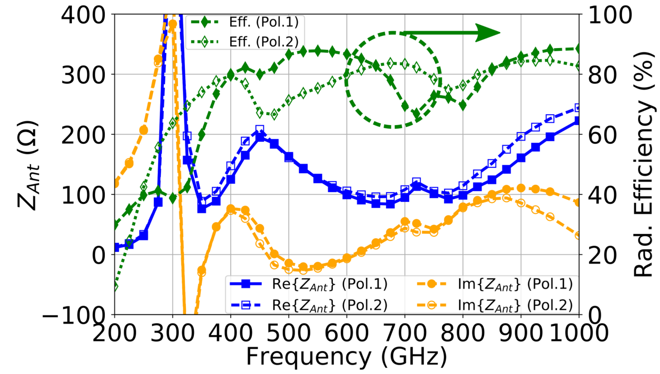

Fig. 13. Full-wave simulated antenna impedance and radiation efficiency for polarizations P1 and P2. It is assumed that the antenna radiates into a silicon half-space through a 150 μm thick lossy silicon substrate.

The impact of the layout-incurred imperfections on the detector performance was investigated with harmonic balance (HB) simulations and compared against the simulation results of the ideal detector circuit from Fig. 3. For the forward-active device operation, the simulated differences are unquantifiable due to the reverse bias of the base-collector junction. In deep saturation, the simulated responsivity drops by no more than a few percent across the entire frequency range of operation. This indicates an essential feature of the chosen detector topology: its robustness to layout-related RF imperfections at the base and collector nodes. In particular, the impact of imperfect termination at the base and collector nodes for the second-order harmonics generated in the rectification process can be practically ignored with the RF fundamental power levels realistically available at THz frequencies. Further, with the optimized antenna-detector layout, the isolation between both polarization paths, P1 and P2, is predominantly defined by the antenna cross-polarization fields. In contrast, the leakage between the base-emitter and base-collector diodes is primarily related to the internal base-emitter capacitance C_{be}, as studied in Section V.

Finally, the combined impact of the serpentine-like dc grounding paths as well as diagonal dc interconnections to the base and collector nodes on the full-wave simulated antenna input impedance and radiation efficiency across 200–1000 GHz is presented in Fig. 13. It is assumed that the antenna radiates into a silicon half-space through a 150 μm thick lossy silicon substrate. Some simulated differences for P1 and P2 are related to the previously discussed layout dissimilarities between both polarization paths. The influence of the complex pixel

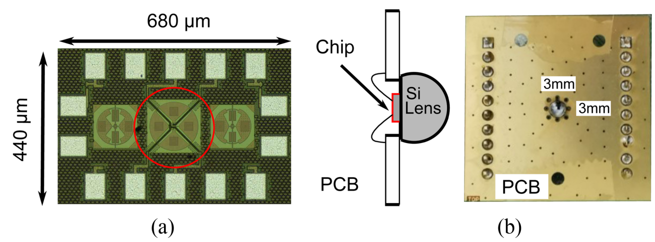

Fig. 14. (a) Detector chip micrograph. (b) Packaged detector chip with 3-mm hyper-hemispherical silicon lens.

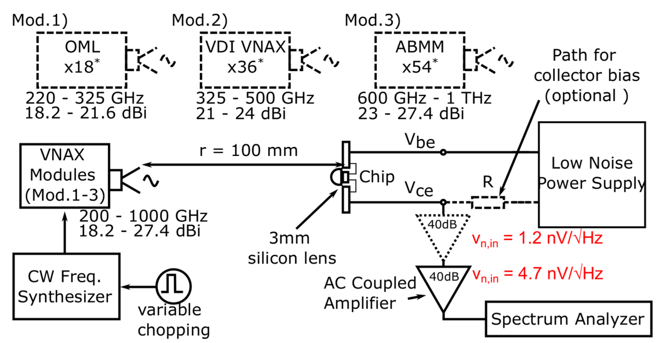

Fig. 15. Detector free-space measurement setup for broadband characterization in a frequency band of 200–1000 GHz.

geometry becomes evident in terms of multiple irregularities in the frequency-dependent impedance and efficiency. With respect to the analysis from Figs. 10 and 11, where the impact of the antenna driving impedance on the detector broadband performance is investigated, an antenna/detector matching efficiency was defined as a ratio of the implemented responsivity to the corresponding ideal responsivity for each separate frequency point. A matching efficiency of at least 80% was found from the detector HB simulations that combined with a high radiation efficiency of around 70–90 % and the theoretical minimum electrical detector NEP of 1.2 pW/$\sqrt{\text{Hz}}$ underlines the theoretical feasibility of THz passive imaging in the investigated device technology.

VII. Detector Characterization in the Frequency Domain

The antenna-coupled detector was assembled with a three-mm diameter hyper-hemispherical silicon lens without AR coating (see Fig. 14) and characterized in the antenna far-field range with three antenna-equipped electronically-chopped precalibrated power extension modules (Mod. 1 – Mod. 3) from OML (WR-3, 220–320 GHz), VDI (WR-2.2, 325–520 GHz), and AB Millimetre (WR-1.2, 620–1000 GHz), as shown in Fig. 15. A frequency range of 520–600 GHz could not be measured because of the missing equipment. A voltage mode readout measuring the detector voltage responsivity R_v was used to facilitate comparison between different device operation regimes. The conversion to the equivalent current responsivity R_i was performed with the aid of additional detector output resistance measurements at dc (see Fig. 5). To minimize the impact of power supply spurs in the LFN spectrum, all important bias points were provided from a low-noise, low-impedance power supply unit from Keysight (B2962 A). To improve the accuracy of noise measurements, in particular for the device in saturation, a set of cascaded low-noise amplifiers (40 dB SR552 from Stanford Research with v_n <1.5 nV/$\sqrt{\text{Hz}}$ followed by 40 dB HVA-10M-60-F from FEMTO) was applied in the readout path. For measurements in the forward-active range (V_{ce} = 1 V) as well as in weak saturation (V_{ce} = 60 mV), each detector path was loaded with a 1.83 kΩ resistor, R_L. Otherwise, the detector output nodes were left unbiased, and no external resistors were applied.

The detector R_v was determined from the Friis transmission equation and the measured directivity of the lens-coupled onchip antenna, the influence of which was deembedded, resulting in the optical detector responsivity that includes all loss mechanisms between free-space and the internal device nodes. In particular, as compared to the previous simulation results, an additional Fresnel loss of around 30% needs to be accounted for as the lens aperture operated without a matching cap. The antenna directivity in each polarization path was determined from direct radiation pattern measurements within a $\pm 50^\circ \times \pm 50^\circ$ sector of the hemisphere [27], [34], [90]. The directivity increases monotonically from 16 to 25.2 dBi across 200–1000 GHz with only minor differences between both orientations.

The NEP was finally calculated from the ratio of detector output noise spectral density and the corresponding responsivity. To minimize the influence of LFN components, the chopping frequency was chosen appropriately in the noise far-out region (at least 1–2 kHz).

A. Detector Responsivity and NEP

An optimum bias point location for all device bias regions was investigated at different RF frequencies. In particular, Fig. 16 presents the bias-dependent detector R_i, R_v, and NEP for three different RF frequencies of 430 GHz, 648 GHz, and 960 GHz. By comparison with the results from Sec, V-B, the measured position of the optimum bias point maximizing R_i as well as its frequency dependence correlates well with the previous simulations. For cold operation ("sat") of the device biased at higher $V_{\rm be}$ values, the discrepancy grows, as expected, due to the previously mentioned device model inaccuracies. As can be noticed, R_i of the detector biased at very low $V_{\rm ce}$ (60 mV) shows only marginal differences compared to the fully-developed forward-active region independently of the operation frequency. For obvious regions (Section IV-B), the corresponding R_v trends for all three bias ranges differ substantially from each other because of an additional output impedance dependence on $V_{\rm bc}$. This, has no impact on the optimum NEP operation point, as can be misleadingly expected. Minimum NEP is located around 760–790 mV, even for deep saturation, and occurs shortly before maximum R_i is achieved. Another interesting conclusion is that the NEP in saturation with practically zero dc-current is never as good as for the forward-active region. The maximum measured R_i appears around 430 GHz and is 1.9 A/W and 6 A/W, for the former and the latter, respectively. The corresponding minimum optical NEP values are 4.3 pW/$\sqrt{\text{Hz}}$ and 2.3 pW/$\sqrt{\text{Hz}}$. The

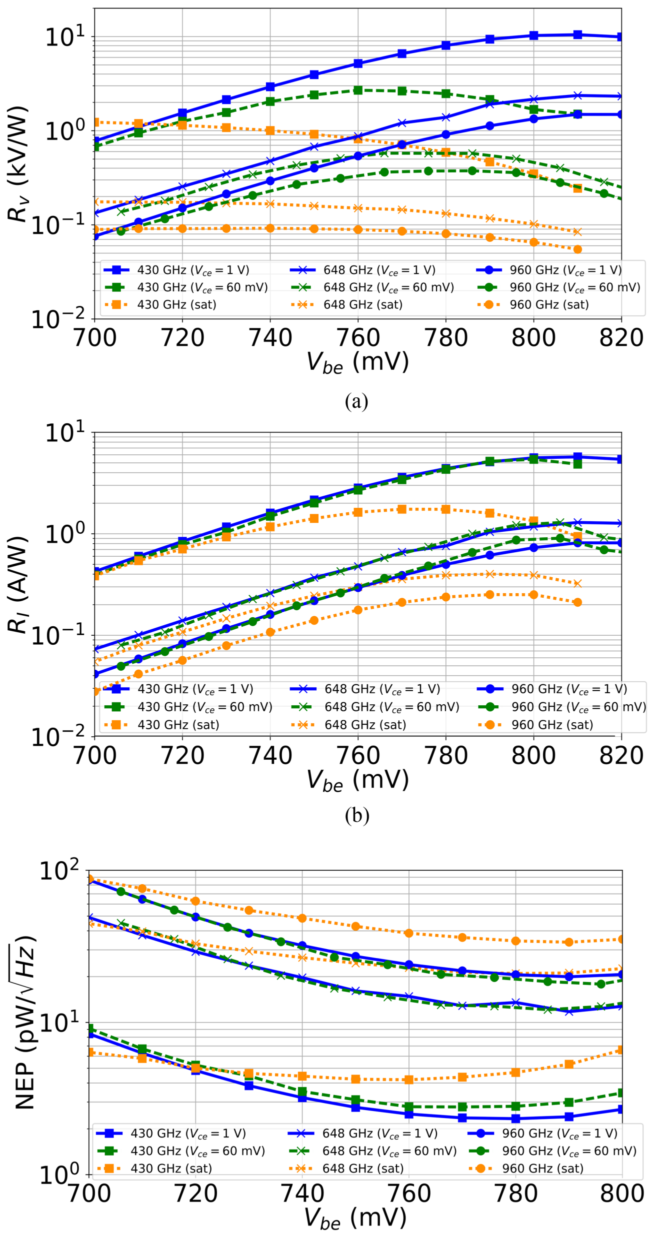

Fig. 16. Bias-dependence of the detector performance measured at three different frequencies: 430 GHz, 648 GHz, and 960 GHz. Voltage responsivity R_v (a), current responsivity R_I (b), and NEP (c). $V_{ce} = 1$ V, $V_{ce} = 60$ mV, and "sat" correspond to the following device bias regions: Forward-active, weak saturation, and deep saturation with the collector nodes left unbiased. The detector spot noise was measured in the far-out region with negligible contributions of LFN components.

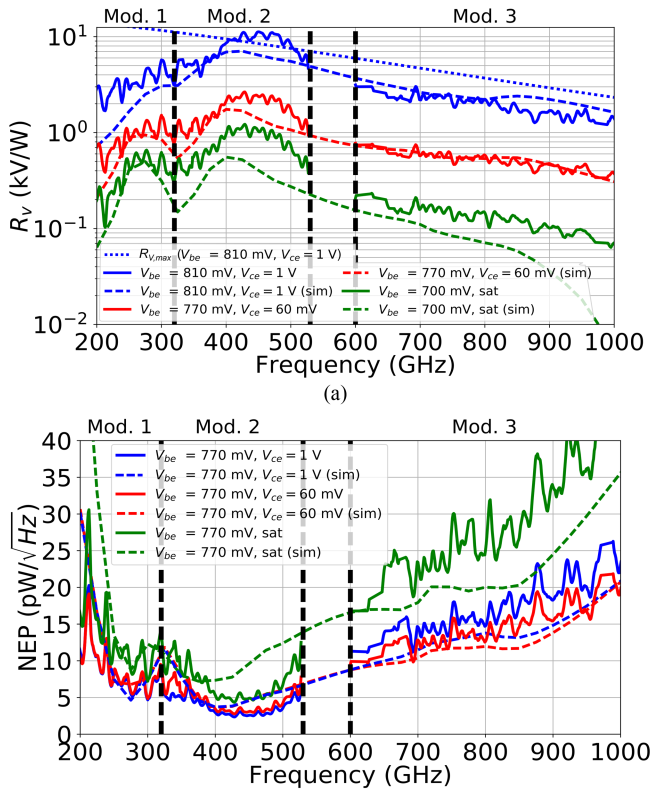

Fig. 17. Frequency dependence of the measured detector voltage responsivity R_v (a) and NEP (b) for three different bias regions ($V_{ce} = 1$ V, $V_{ce} = 60$ mV, and saturation). $R_{v,\max}$ denotes the maximum detector R_v simulated with the optimum antenna impedance including 30% Fresnel loss. The detector spot noise was measured in the far-out region of its spectral density. The plots are given for one polarization. The corresponding R_v and NEP for the second polarization path do not deviate by more than 10%.

RF frequency roll-off of the measured and simulated maximum detector voltage responsivity, R_v, and minimum NEP for three different bias regions is gathered in Fig. 17. Please note that different bias points were chosen for the plots maximizing R_v in each distinct bias range. Contrary to that, a single bias point with V_{be} of 770 mV was chosen for all curves, which minimizes the detector NEP in a broad sense independently from the operation range. According to Fig. 16, additional NEP optimization is possible at higher RF frequencies with an additional increase of V_{be}. An excellent model-hardware correlation, typically within 1–2 dB, was achieved across 200–1000 GHz for the detector biased in all investigated operating regions. The highest discrepancy is found for deep saturation due to the lowest model accuracy. As a reference, an additional dotted curve is plotted in Fig. 17(a). It corresponds to the maximum achievable detector responsivity (forward-active region) with the optimum antenna driving impedance, according to Fig. 10, and an ideal antenna radiation efficiency into a silicon substrate. Only a 30% Fresnel loss resulting from the uncoated lens aperture is included in the calculation. A frequency roll-off of the reference curve confirms a near-optimum detector operation across multiple hundred GHz.

In the simulated curves, two distinctive corner frequencies can be noticed around 450 GHz and 900 GHz. They can be traced back to an aggregate impact of R_b, R_e, and C_{be}, as studied in Section V. Although the first of them can be easily identified in the measured curves with some shift toward 520 GHz, the other is not easily found, which may be attributed to the frequency limitations of the applied device model. In deep saturation, the measured NEP is, on average, two times higher than for the forward-active operation. Due to the relatively weak frequency slope of the detector responsivity toward higher frequencies, a classical three-dB RF bandwidth definition does not provide the correct metric quantifying the detector sensitivity in a broadband sense. Therefore, the detector equivalent noise bandwidth, B_{eq}, was calculated from the measured responsivity, according to the following [13], [15]:

$$B_{\text{eq}} = \frac{[\int_0^\infty R_v(f)\, df]^2}{\int_0^\infty R_v(f)^2\, df}. \tag{3}$$

Similarly, the detector equivalent responsivity, $R_{v,\text{eq}}$, with the corresponding equivalent NEP_{eq} can be further found as

$$R_{v,\text{eq}} = \frac{\int_0^\infty R_v(f)^2\, df}{\int_0^\infty R_v(f)\, df} \tag{4}$$

and

$$NEP_{\text{eq}} = \frac{v_n}{R_{v,\text{eq}}} \tag{5}$$

where v_n is the voltage noise spectral density at the detector output. With the NEP-optimum base bias point of around 770 mV, B_{eq}, $R_{v,\text{eq}}$, and NEP_{eq} are 512 GHz, 3.29 kV/W, and 4.7 pW/$\sqrt{\text{Hz}}$, correspondingly, for each separate detection path operated in the forward-active range. The data was interpolated from the measured curves for the missing frequency range of 520–600 GHz.

Having calculated the detector equivalent parameters from above, the resulting NETD can be finally found from the following relation, which is equivalent to (1)

$$NETD = \frac{v_n}{k_B \int_{-\infty}^{\infty} R_v(f)\, df} \cdot \frac{1}{\sqrt{2\tau_{\text{int}}}} \tag{6}$$

and is equal to 0.67 K in the far-out range of the noise spectral density with negligible impact of LFN components.

VIII. Broadband Detector Characterization With Black-Body Source

Direct measurements with a broadband black-body standard present an ultimate characterization step of the detector performance. Here, several quite involved deembedding steps from the previous RF CW setup can be eliminated. At the same time, new loss factors related to optical coupling efficiency (spillover, Gaussisity) of the black-body radiation appear that need to be properly addressed. A key requirement for accurate detector characterization in this measurement setup is the availability of the uniformly distributed frequency-independent power spectral density across a field-of-view of the lens-coupled detector, which is ideally equal to $k_B T$ in the Rayleigh-Jeans approximation of Planck's law. For that purpose, an optical train made of two elliptical mirrors (11.3 cm×16.3 cm, f=18.75 cm, f/1.5), as shown in Fig. 18, was used to focus the black-body emission onto the lens aperture. Under such illumination conditions, the detector thermal responsivity, $R_v(T)$, can be directly measured and related to the frequency-dependent voltage responsivity, $R_v(f)$, as

$$R_v(T) = \frac{\partial V_{\text{out}}}{\partial T} \int_{-\infty}^{\infty} k_B T \cdot R_v(f)\, df = k_B \int_{-\infty}^{\infty} R_v(f)\, df \tag{7}$$

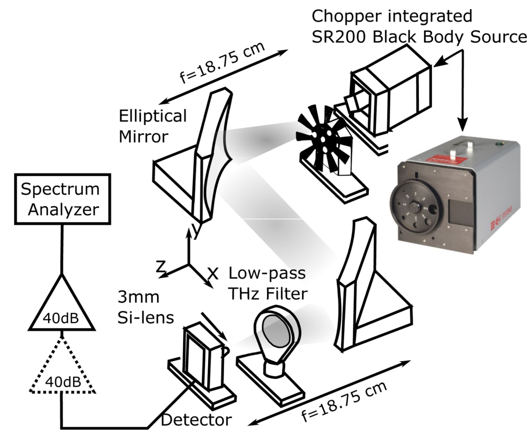

Fig. 18. Broadband detector characterization setup with a reference black-body standard. The setup includes two elliptical mirrors focusing the thermal emission onto the detection plane and an additional 1.50 THz low-pass multi-mesh filter to block the dominant IR background.

where V_{out} denotes the measured voltage response at the detector output. Finally, 1-Hz NETD can be calculated as $v_n/R_v(T) \cdot \sqrt{Hz}$ which is equal to (6).

A reference cavity black-body from CI Systems (SR-200 N) was used as a broadband source of thermal emission. It is equipped with an adjustable aperture size (0.8–22.2 mm diameter) and a mechanically-chopped blade. The chopping speed is limited to a lower kHz range and traded against the aperture size. It can be operated in a temperature range from 50 °C to 1200 °C with an absolute accuracy of 0.5 K. To maximize the measurement accuracy, the entire setup was covered with absorbing material (AN-72 from Eccosorb). To avoid the influence of IR emission on the detector response, a low-pass multimesh filter from QMC Instruments with a cut-off frequency of 1.5 THz and a typical out-of-band rejection of 30 dBc was applied in close-proximity of the lens aperture. The filter in-band transmission was characterized (85%) and its impact deembedded from the consecutive set of detector measurements as well as the chopping factor of $\sqrt{2}/\pi \approx 0.45$ [91].

The black-body and the lens-coupled detector were initially positioned in the focal points of the corresponding mirrors and the entire optical train was aligned to maximize the detector response. The Gaussicity of the lens-coupled antenna was estimated experimentally from the previously measured radiation patterns and was calculated between 85% and 90% for 250–900 GHz. An aperture size of 9.5 mm was applied to achieve the most uniform illumination at the lens aperture while supporting an adequate chopping frequency of 1.5 kHz. To verify the uniformity of illumination pattern across the physical lens aperture (3 mm diameter), the antenna-coupled detector was scanned in 2-D along the detection plane. The acquired normalized light intensity profile is shown in Fig. 19, indicating a well-defined power distribution with a minor signal drop of 0.25 dBV at 1.5 mm offset from the center which corresponds to the lens physical boundaries. This signal drop was deembedded in a postprocessing step of the measured detector thermal responsivity, $R_v(T)$.

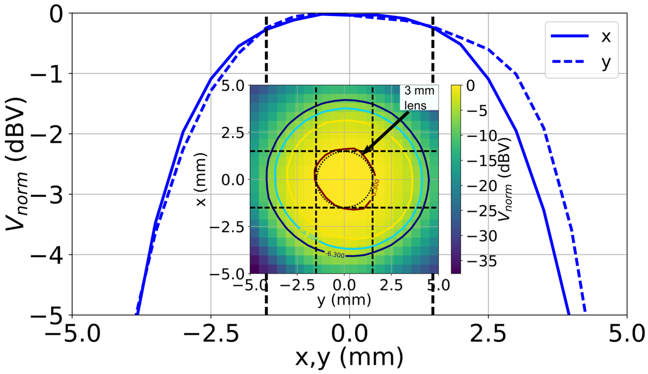

Fig. 19. 2-D scan of the power density in the detection plane while illuminated with a 9.5 mm black-body aperture at 1000 °C. An output signal from two polarization paths, P1 and P2, was recorded simultaneously to capture the full intensity of unpolarized light from the black-body.

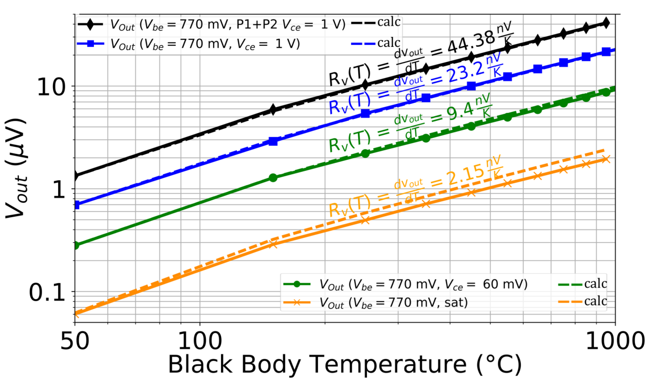

Fig. 20. Detector voltage response versus black-body temperature for three distinct detector bias ranges. $V_{\rm be}$=770 mV corresponds to the minimum NEP operation. The resulting detector thermal sensitivity $R_v(T)$ is also indicated. The total voltage response calculated ("–calc") based on the measured frequency-dependent $R_v(f)$ is further given for comparison purposes.

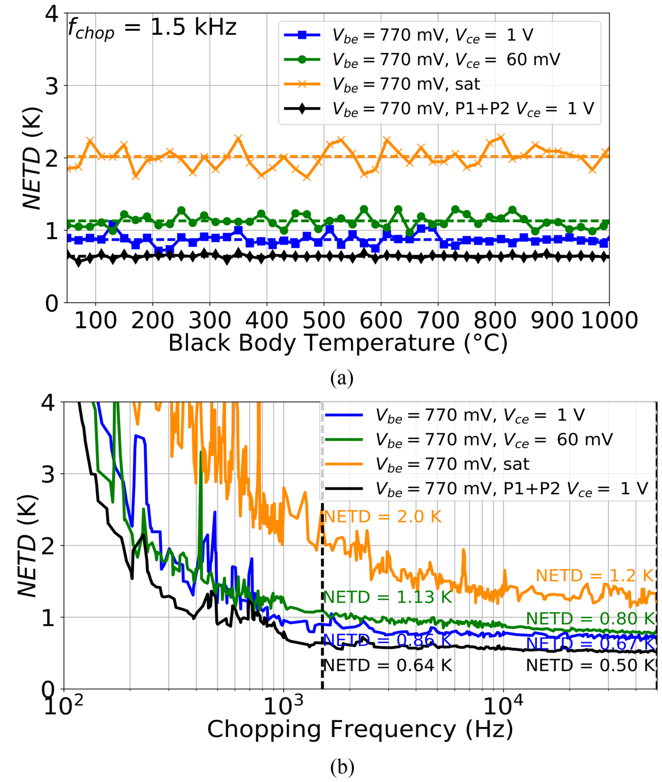

Fig. 21. Measured NETD (1-Hz bandwidth) across three distinct detector bias ranges. (a) NETD at 1.5-kHz offset frequency versus black-body temperature, (b) NETD spectral density.

The same readout scheme as in the previous CW characterization setup was applied here. Additional measurements with an aggregate response from two paths running simultaneously, denoted as P1+P2, were performed to investigate the full detector functionality for an operation with unpolarized light. In this case, two detector outputs were pulled to the same 1.83 kΩ load resistor.

A. Thermal Sensitivity and NETD

The detector voltage response, $V_{\rm out}$, was measured for 50 °C–1000 °C and the corresponding thermal responsivity, $R_v(T)$, was found from the slope $dV_{\rm out}/dT$, as presented in Fig. 20 for the base-emitter bias voltage of 770 mV. $V_{\rm be}$=770 mV was found to provide the minimum NETD correlating well with the previous CW characterization results (see Fig. 16). Near ideal linear $V_{\rm out}$ dependence on the black-body temperature indicates the detector linear operation up to the highest measured value of 1000 °C. All three previously studied device bias regions, from deep saturation to forward-active, were characterized, resulting in different $R_v(T)$ values from 2.15 nV/K to 23.2 nV/K. Simultaneous forward-active operation of both paths (P1+P2) results in a total responsivity of 44.4 nV/K, which indicates a nearly identical response along both polarization planes. The $R_v(T)$ values calculated from the CW measurements according to (7) are further plotted ("calc") for comparison. Both values correlate very well, thus validating both measurement approaches. The highest discrepancy, although still small (below 1 dB), occurs for the detector in deep saturation. Despite some additional coupling losses in the broadband measurement setup, $R_v(T)$ measured for the forward-active bias range is practically the same for both characterization methods. The major source of this indirect discrepancy may be attributed to the fact that $R_v(f)$ for 520–600 GHz was only interpolated. The other error sources may be further related to a limited accuracy in defining the antenna directivity and the radiated output power of the precalibrated power extension modules. The directly measured $R_v(T)$, in combination with the measured noise floor, v_n, was further applied to calculate the NETD (one-Hz bandwidth) with the most relevant results presented in Fig. 21. As expected, the detector NETD is practically invariant to the temperature change as a direct consequence of its linear operation. From the measured spectral density of NETD, the minimum NETD values achievable in the far-out range of the noise spectrum vary from 0.67 K for the forward-active operation up to 1.2 K in deep saturation, correlating very well with the corresponding numbers calculated in the previous section from the CW

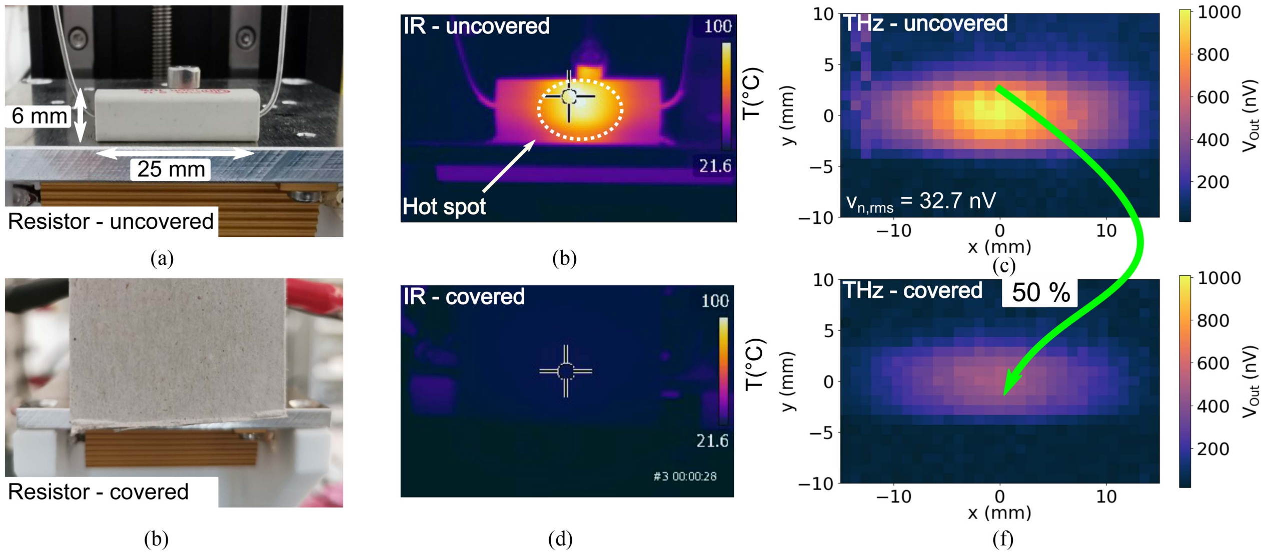

Fig. 22. Various images of the raster-scanned 100 °C hot resistor (not to scale): (a) Visible image. (b) Visible image covered by cardbox (0.4 mm). (c) IR image. (d) IR image through cardbox. (e) THz image. (f) THz image through cardbox.

measurement results. Simultaneous operation of two paths scales the NETD value from 0.67 K down to 0.5 K, indicating near zero-correlation between both detection paths.

Interesting to notice is that the forward-active operation supports a near-minimum NETD at offset frequencies of around 1–2 kHz while the cold bias (saturation) fails despite a near-zero device bias current. This behavior, although at first glance possibly unclear, becomes well understood in view of the experimental noise analysis results from Section IV-B. In particular, for the chopping frequency of 1.5 kHz in the black-body measurement setup, the 1-Hz NETD values scale up to 0.86 K and 2 K, while operated in the forward-active range and in saturation, correspondingly. Simultaneous dual-path operation supports 0.64 K NETD under similar chopping conditions.

IX. Imaging Experiment

An imaging experiment was performed to verify the basic capability of the detector to operate with passive illumination. The experiment refers to the previous black-body measurement setup from Fig. 18, the only difference is that the reference emission is replaced with a 25 mm $\times$ 6 mm large, 10 Ω, ceramic resistor which is heated up to 100 $^\circ$ C by a dc current, as shown in Fig. 22. The resistor was assembled on a linear translational stage and raster-scanned with a step size of 1 mm while recording the rectified output voltage from both polarization paths (P1+P2) pulled to the same load resistance. To calibrate the THz images acquired by the detector, IR images were taken with a reference camera (FLIR T450sc with NETD $\leq$30 mK), indicating a maximum and a minimum temperature of 100 °C and 21.8 °C, respectively, within the same frame. In the next step, the resistor was covered with an optically opaque, 0.4-mm thick cardbox and another picture was taken. An additional distance of around 5 cm between both was applied, to minimize the cardbox heating by the resistor. As compared to the IR image, where the cardbox practically hides the resistor, the covered object can still be identified in THz image with a signal reduction of around 50 %, clearly showing the see-through ability of thermal emission in the frequency band below 1 THz.

The next step was to map the absolute signal values recorded in the image onto the detector performance metrics from Figs. 20 and 21. Considering the previously measured detector thermal responsivity, $R_v(T)$, of 44.38 nV/K, the chopping factor of $\sqrt{2}/\pi$, an assumed typical ceramic emissivity of ≈ 0.9 [92], and an additional geometrical fill factor of ≈ 0.8 at the lens aperture, the following maximum signal value for the 100°C hot resistor is expected: 1.12 μV. This matches very well the measured peak value of 1.01 μV. The fill factor is related to limited vertical resistor size compared to the reference black-body aperture size ($\phi = 9.5$ mm). Concerning Fig. 19, one can notice that at least that aperture size is needed with the used optical train to reach the maximum detector response. The fill factor is calculated as surface ratio of the resistor hot spot defined from the IR camera and the black-body aperture. Of course, this only represents a very coarse estimation of the real illumination conditions which are far from being uniform.

Performing similar reasoning and noting that the rms noise floor in the captured image is around 32.7 nV, an equivalent NETD (1-Hz bandwidth) of around 0.82 K was calculated, which once again compares well with the reference value of 0.64 K from Fig. 21.

X. Conclusion

A systematic study of the application potential as well as the technology-driven performance limitations of the modern SiGe HBT devices for broadband passive room-temperature detection in the lower THz range was presented in this work and compared to the currently available state-of-the-art. In view of the requirement for a full array scalability, only a small form-factor, low-power operated, antenna-coupled direct detector architecture without preamplification was considered. Due to limitations of the current active technologies in terms of the achievable maximum THz responsivity and minimum noise floor, a sub-Kelvin NETD detector operation translates into the required noise-equivalent bandwidth of at least a few hundred GHz. To achieve this goal, the antenna-detector codesign aspects with an in-depth understanding of the impact of internal device parasitics on the frequency-dependent rectification process are crucial. For that purpose, a simplified nonlinear high-frequency detector model was applied which is valid for the device operating not only in the forward-active region but also in deep saturation (cold operation). With the aid of this model, all major response degradation mechanisms at THz frequencies independently from the bias range were investigated, with two major aspects highlighted below. First, the series-feedback emitter contact resistance R_e linearizes the detector and is the primary source of the static responsivity degradation. Second, the contact resistances R_b and R_c prevent ac grounds (for the fundamental frequency) at the internal nodes resulting in a fundamental RF voltage swing at the base-collector diode, which frequency-dependently increases due to the shunting action of $C_{\rm be}$. All bias-dependent device parasitics result in a theoretically achievable technology-driven upper-limited detector performance manifesting in a minimum electrical NEP of 1.2 pW/$\sqrt{\rm Hz}$ at 300 GHz that increases towards 10.5 pW/$\sqrt{\rm Hz}$ at 1 THz. Knowing the global performance limit, the matching efficiency of the proposed detector implementation for broadband rectification was evaluated across a near-THz band and found to be at least 80 %. Equally important for minimum NEP is a proper understanding and experimental verification of the device noise mechanisms not only in the far-our range but also at low dc-offset frequencies (LFN). The location of the effective LFN corner frequency is particularly relevant for practical detector implementations. Even though the detectors are operated at very low-bias currents, considerably below those corresponding to the maximum device speed, the G-R noise was found to be a limiting factor concerning this operation aspect. More important, the impact of G-R noise was more important for the cold-operated device, although the overall far-out noise floor was lower than for the forward-active operation.

Apart from the detailed detector theoretical study, a comprehensive analysis of various practical challenges related to the implementation of small form-factor, silicon-integrated THz direct detectors for broadband operation with unpolarized light was presented. These challenges are mostly layout-incurred and refer to a dual-channel multiport excitation within a single concentric antenna layout. They impact the requested near 1-THz RF bandwidth and the inherent circuit symmetries. These symmetries are crucial for the ideal detector driving conditions as they provide superior dc-to-RF isolation as well as low leakage rate between both polarization paths.

The complete detecting pixel was implemented in a modern high-speed 130 nm SiGe HBT technology with $f_t/f_{\rm max}$ of 470/650 GHz. It includes two independent polarization paths within a single dual-polarization lens-coupled onchip antenna with the close-to-optimum performance in a near-THz fractional bandwidth and the deembedded equivalent noise bandwidth of 512 GHz centered around 430 GHz. The detector optical NEP for each independent polarization path was measured across 200–1000 GHz reporting state-of-the-art values of 2.3–23 pW/$\sqrt{\rm Hz}$ and 4.3–45 pW/$\sqrt{\rm Hz}$ with the device operating in the forward-active range and in saturation, respectively. Here, the detector noise floor in the far-out range was assumed in the calculations. Final verification of the detector broadband operation was performed in a focused measurement setup with a cavity black-body standard chopped mechanically at 1.5 kHz, demonstrating a 1-Hz defined optical NETD of 0.86 K and 2 K in each separate polarization path for the device biased in the forward-active range and in saturation, respectively. With the simultaneous operation of two channels, the NETD scaled down to 0.64 K, indicating near-zero noise correlation between both polarization paths. This number can be potentially reduced to around 0.5 K if operated in the far-out range of the detector noise floor. To verify the capability of the detector to operate with passive illumination, an imaging experiment in a raster-scanned setup was performed, comparing well to the reference NETD values determined from both the RF and the black-body characterization setup. Even though a sub-Kelvin NETD was demonstrated with the present detector implementation, true video-rate imaging, available with preamplified detectors in the lower frequency range, is still out of reach without further technology developments.

References

[1] K. Rautiainen et al., "L-band radiometer observations of soil processes in boreal and subarctic environments," *IEEE Trans. Geosci. Remote Sens.*, vol. 50, no. 5, pp. 1483–1497, May 2012.

[2] R. Knipper et al., "THz absorption in fabric and its impact on body scanning for security application," *IEEE Trans. THz Sci. Technol.*, vol. 5, no. 6, pp. 999–1004, Nov. 2015.

[3] L. Yujiri, M. Shoucri, and P. Moffa, "Passive millimeter wave imaging," *IEEE Microw. Mag.*, vol. 4, no. 3, pp. 39–50, Sep. 2003.

[4] M. Planck and M. Masius, *The Theory of Heat Radiation*. Philadelphia, PA, USA: Blakiston's Son and Co, 1914.

[5] G. P. Kniffin and L. M. Zurk, "Model-based material parameter estimation for terahertz reflection spectroscopy," *IEEE Trans. THz Sci. Technol.*, vol. 2, no. 2, pp. 231–241, Mar. 2012.

[6] A. Timofeev et al., "Optical and electrical characterization of a large kinetic inductance bolometer focal plane array," *IEEE Trans. THz Sci. Technol.*, vol. 7, no. 2, pp. 218–224, Mar. 2017.

[7] M. Tiuri, "Radio astronomy receivers," *IEEE Trans. Antennas Propag.*, vol. 12, no. 7, pp. 930–938, Dec. 1964.

[8] C. Dietlein et al., "Phenomenology of passive broadband terahertz images," in *Proc. ESA Workshop Millimetre-wave Technol. Appl.*, Jan. 2006, pp. 405–410.

[9] A. Luukanen, A. Miller, and E. Grossman, "Passive hyperspectral terahertz imagery for security screening using a cryogenic microbolometer," in *Proc. SPIE's Secur. Defence Symp.*, May 2005, pp. 127–134.

[10] E. N. Grossman, K. Leong, X. Mei, and W. Deal, "Low-frequency noise and passive imaging with 670 GHz HEMT low-noise amplifiers," *IEEE Trans. THz Sci. Technol.*, vol. 4, no. 6, pp. 749–752, Nov. 2014.

[11] C. M. Cooke et al., "A 670 GHz integrated InP HEMT direct-detection receiver for the tropospheric water and cloud ice instrument," *IEEE Trans. THz Sci. Technol.*, vol. 11, no. 5, pp. 566–576, Sep. 2021.

[12] J. J. Lynch et al., "Passive millimeter-wave imaging module with preamplified zero-bias detection," *IEEE Trans. Microw. Theory Techn.*, vol. 56, no. 7, pp. 1592–1600, Jul. 2008.

[13] E. Dacquay et al., "D-band total power radiometer performance optimization in an SiGe HBT technology," *IEEE Trans. Microw. Theory Techn.*, vol. 60, no. 3, pp. 813–826, Mar. 2012.

[14] T. Kanar and G. M. Rebeiz, "A low-power 136-GHz SiGe total power radiometer with NETD of 0.25 k," *IEEE Trans. Microw. Theory Techn.*, vol. 64, no. 3, pp. 906–914, Mar. 2016.

[15] R. B. Yishay and D. Elad, "A 95–135 GHz low power dicke radiometer in SiGe BiCMOS technology," in *Proc. 2020 15th Eur. Microw. Integr. Circuits Conf. (EuMIC)*, 2021, pp. 133–136.

[16] E. Turkmen, B. Cetindogan, M. Yazici, and Y. Gurbuz, "Design and characterization of a D-band SiGe HBT front-end for dicke radiometers," *IEEE Sens. J.*, vol. 20, no. 9, pp. 4694–4703, May 2020.

[17] Q. J. Gu, Z. Xu, A. Tang, and M.-C. Frank Chang, "A D-band passive imager in 65 nm CMOS," *IEEE Microw. Wireless Compon. Lett.*, vol. 22, no. 5, pp. 263–265, May 2012.

[18] B. Ustundag et al., "Front-end blocks of a W-band dicke radiometer in SiGe BiCMOS technology," *IEEE Trans. Circuits Syst. II Exp. Briefs*, vol. 67, no. 11, pp. 2417–2421, Nov. 2020.

[19] L. Gilreath, V. Jain, and P. Heydari, "Design and analysis of a W-band SiGe direct-detection-based passive imaging receiver," *IEEE J. Solid-State Circuits*, vol. 46, no. 10, pp. 2240–2252, Oct. 2011.

[20] A. Tang, Y. Kim, and Q. J. Gu, "25.4 A 0.43K-noise-equivalent-Δ t 100 GHz dicke-free radiometer with 100% time efficiency in 65 nm CMOS," in *Proc. IEEE Int. Solid-State Circuits Conf.*, 2016, pp. 430–431.

[21] J. Grzyb et al., "An on-chip antenna-coupled preamplified D-band to J-band total power radiometer chip in 130 nm SiGe BiCMOS technology," in *Proc. 2024 IEEE Radio Freq. Integr. Circuits Symp.*, Jun. 2024, pp. 430–431.

[22] D. Becker et al., "High-resolution passive video-rate imaging at 350 GHz," in *Passive Millimeter-Wave Imaging Technology XIV*, vol. 8022, Bellingham, WA, USA: SPIE, 2011.

[23] E. Heinz et al., "Passive submillimeter-wave stand-off video camera for security applications," *J. Infrared, Millimeter, THz Waves*, vol. 31, no. 11, pp. 1355–1369, Sep. 2010.

[24] A. Luukanen and J. P. Pekola, "A superconducting antenna-coupled hot-spot microbolometer," *Appl. Phys. Lett.*, vol. 82, no. 22, pp. 3970–3972, May 2003.

[25] R. A. Lewis, "A review of terahertz detectors," *J. Phys. D Appl. Phys.*, vol. 52, no. 43, Aug. 2019, Art. no. 433001.

[26] S. Ariyoshi et al., "Terahertz imaging with a direct detector based on superconducting tunnel junctions," *Appl. Phys. Lett.*, vol. 88, no. 20, May 2006.

[27] M. Andree et al., "A broadband antenna-coupled terahertz direct detector in a 0.13-μm SiGe HBT technology," in *Proc. 2019 14th Eur. Microw. Integr. Circuits Conf. (EuMIC)*, 2019, pp. 168–171.

[28] M. Andree, J. Grzyb, R. Jain, B. Heinemann, and U. R. Pfeiffer, "Broadband modeling, analysis, and characterization of SiGe HBT terahertz direct detectors," *IEEE Trans. Microw. Theory Techn.*, vol. 70, no. 2, pp. 1314–1333, Feb. 2022.

[29] E. Shaulov, S. Jameson, and E. Socher, "A zero bias J-band antenna-coupled detector in 65-nm CMOS," *IEEE Trans. THz Sci. Technol.*, vol. 11, no. 1, pp. 62–69, Jan. 2021.

[30] J. Sun et al., "Passive terahertz imaging detectors based on antenna-coupled high-electron-mobility transistors," *Opt. Exp.*, vol. 28, no. 4, pp. 4911–4920, Feb. 2020.

[31] T. Watanabe et al., "Ultrahigh sensitive plasmonic terahertz detector based on an asymmetric dual-grating gate HEMT structure," *Solid-State Electron.*, vol. 78, pp. 109–114, 2012.

[32] S. V. Berkel et al., "Wideband modeling of CMOS schottky barrier diode detectors for THz radiometry," *IEEE Trans. THz Sci. Technol.*, vol. 11, no. 5, pp. 495–507, Sep. 2021.

[33] S. van Berkel, O. Yurduseven, A. Freni, A. Neto, and N. Llombart, "THz imaging using uncooled wideband direct detection focal plane arrays," *IEEE Trans. THz Sci. Technol.*, vol. 7, no. 5, pp. 481–492, Sep. 2017.

[34] J. Grzyb, M. Andree, R. Jain, B. Heinemann, and U. R. Pfeiffer, "A lens-coupled on-chip antenna for dual-polarization SiGe HBT THz direct detector," *IEEE Antennas Wireless Propag. Lett.*, vol. 18, no. 11, pp. 2404–2408, Nov. 2019.

[35] J. Grzyb et al., "Real-time video rate imaging with a 1k-pixel THz CMOS focal plane array," in *Passive and Active Millimeter-Wave Imaging XV*, vol. 8362, Bellingham, WA, USA: SPIE, 2012, pp. 86–97.

[36] R. Al Hadi et al., "A 1 k-pixel video camera for 0.7–1.1 terahertz imaging applications in 65-nm CMOS," *IEEE J. Solid-State Circuits*, vol. 47, no. 12, pp. 2999–3012, Dec. 2012.

[37] S. Yokoyama et al., "5.8 A 32×32-Pixel 0.9THz Imager with pixel-parallel 12b VCO-based ADC in 0.18 M CMOS," in *Proc. IEEE Int. Solid-State Circuits Conf.*, 2019, pp. 108–110.

[38] Z.-Y. Liu, L.-Y. Liu, J. Yang, and N.-J. Wu, "A CMOS fully integrated 860-GHz terahertz sensor," *IEEE Trans. THz Sci. Technol.*, vol. 7, no. 4, pp. 455–465, Jul. 2017.

[39] Q. Yang, X. Ji, Y. Xu, and F. Yan, "Improved performance of CMOS terahertz detectors by reducing MOSFET parasitic capacitance," *IEEE Access*, vol. 7, pp. 9783–9789, 2019.

[40] U. R. Pfeiffer, J. Grzyb, H. Sherry, A. Cathelin, and A. Kaiser, "Toward Low-NEP room-temperature THz MOSFET direct detectors in CMOS technology," in *Proc. Int. Conf. Infrared Millimeter Terahertz Waves*, Sep. 2013, pp. 1–2.

[41] R. Jain et al., "A terahertz direct detector in 22 nm FD-SOI CMOS," in *Proc. 2018 13th Eur. Microw. Integr. Circuits Conf. (EuMIC)*, 2018, pp. 25–28.

[42] D. Y. Kim, S. Park, and R. Han, "Design and demonstration of 820-GHz array using diode-connected NMOS transistors in 130-nm CMOS for active imaging," *IEEE Trans. THz Sci. Technol.*, vol. 6, no. 2, pp. 306–317, Mar. 2016.

[43] C. Chen, R. A. Hadi, and M.-C. F. Chang, "Antenna-coupled terahertz detectors in 16 nm FinFET," in *Proc. 2023 IEEE/MTT-S Int. Microw. Symp.*, 2023, pp. 574–577.

[44] W. Shockley, "The theory of p-n junctions in semiconductors and p-n junction transistors," *Bell Syst. Tech. J.*, vol. 28, no. 3, pp. 435–489, 1949.

[45] I. Mehdi, J. V. Siles, C. Lee, and E. Schlecht, "THz diode technology: Status, prospects, and applications," in *Proc. IEEE*, vol. 105, no. 6, pp. 990–1007, Jun. 2017.

[46] Keng L Fong and R. G. Meyer, "High-frequency nonlinearity analysis of common-emitter and differential-pair transconductance stages," *IEEE J. Solid-State Circuits*, vol. 33, no. 4, pp. 548–555, Apr. 1998.

[47] Z. Ahmad and K. K. O, "THz detection using p /n-well diodes fabricated in 45-nm CMOS," *IEEE Electron Device Lett.*, vol. 37, no. 7, pp. 823–826, Jul. 2016.

[48] R. Han et al., "Active terahertz imaging using schottky diodes in CMOS: Array and 860-GHz pixel," *IEEE J. Solid-State Circuits*, vol. 48, no. 10, pp. 2296–2308, Oct. 2013.

[49] N. Shabanzadeh et al., "A study of the effects limiting the responsivity of a broadband THz power detector with on-chip antenna in $0.13\mu m$ SiGe HBT technology," in *Proc. 2022 IEEE Nordic Circuits Syst. Conf. (NorCAS)*, 2022, pp. 1–5.

[50] R. Al Hadi, J. Grzyb, B. Heinemann, and U. R. Pfeiffer, "A terahertz detector array in a SiGe HBT technology," *IEEE J. Solid-State Circuits*, vol. 48, no. 9, pp. 2002–2010, Sep. 2013.

[51] M. Andree, J. Grzyb, R. Jain, B. Heinemann, and U. R. Pfeiffer, "A broadband dual-polarized terahertz direct detector in a 0.13-μm SiGe HBT technology," in *Proc. IEEE Int. Microw. Symp. Conf.*, Jun. 2019, pp. 500–503.

[52] J. Grzyb, M. Andree, B. Heinemann, H. Rücker, and U. R. Pfeiffer, "On cold operation of an SiGe HBT as a broadband Low-NEP THz direct detector," in *Proc. 2023 48th Int. Conf. Infrared Millimeter Terahertz Waves (IRMMW-THz)*, 2023, pp. 1–2.

[53] R. L. Schmid, A.Ç. Ulusoy, P. Song, and J. D. Cressler, "A 94 GHz 1.4 dB insertion loss single-pole double-throw switch using reverse-saturated SiGe HBTs," *IEEE Microw. Wireless Compon. Lett.*, vol. 24, no. 1, pp. 56–58, Jan. 2014.

[54] R. L. Schmid, P. Song, C. T. Coen, A.Ç. Ulusoy, and J. D. Cressler, "On the analysis and design of low-loss single-pole double-throw W-band switches utilizing saturated SiGe HBTs," *IEEE Trans. Microw. Theory Techn.*, vol. 62, no. 11, pp. 2755–2767, Nov. 2014.

[55] D. Cetindogan et al., "A D-band SPDT switch utilizing reverse-saturated SiGe HBTs for dicke-radiometers," in *Proc. 2018 German Microw. Conf.(GeMiC)*, Freiburg, Germany, Mar. 2018, pp. 47–50.

[56] I. Song et al., "An investigation on the use of inverse-mode SiGe HBTs as switching pairs for SET-mitigated RF mixers," *IEEE Trans. Nucl. Sci.*, vol. 63, no. 2, pp. 1099–1108, Apr. 2016.

[57] W. Liang et al., "96 GHz 4.7 mW low-power frequency tripler with 0.5 V supply voltage," *Electron. Lett.*, vol. 53, no. 19, pp. 1308–1310, Sep. 2017.

[58] S. Seth, C. H. J. Poh, T. Thrivikraman, R. Arora, and J. D. Cressler, "Using saturated SiGe HBTs to realize ultra-low voltage/power X-band low noise amplifiers," in *Proc. 2011 IEEE Bipolar/BiCMOS Circuits Techn. Meet. (BCTM)*, Atlanta, USA, Oct. 2011, pp. 103–106.

[59] P. Pursula et al., "Integrated radiometer at 240 GHz with SiGe MMIC detector and GRIN silicon lens," *IEEE Trans. Microw. Theory Techn.*, vol. 72, no. 6, pp. 3505–3513, Jun. 2024.

[60] K. Sengupta, D. Seo, L. Yang, and A. Hajimiri, "Silicon integrated 280 GHz imaging chipset with 4 SiGe receiver array and CMOS source," *IEEE Trans. THz Sci. Technol.*, vol. 5, no. 3, pp. 427–437, May 2015.

[61] D. Yoon et al., "300-GHz direct and heterodyne active imagers based on 0.13-μm SiGe HBT technology," *IEEE Trans. THz Sci. Technol.*, vol. 7, no. 5, pp. 536–545, Sep. 2017.

[62] M. Uzunkol, O. D. Gurbuz, F. Golcuk, and G. M. Rebeiz, "A 0.32 THz SiGe 4x4 imaging array using high-efficiency on-chip antennas," *IEEE J. Solid-State Circuits*, vol. 48, no. 9, pp. 2056–2066, Sep. 2013.
[63] D. Corcos et al., "Antenna-coupled MOSFET bolometers for uncooled THz sensing," *IEEE Trans. THz Sci. Technol.*, vol. 5, no. 6, pp. 902–913, Nov. 2015.
[64] A. Svetlitza et al., "CMOS-SOI-MEMS thermal antenna and sensor for uncooled THz imaging," *IEEE Trans. Electron Devices*, vol. 63, no. 3, pp. 1260–1265, Mar. 2016.
[65] D. Čibiraitė et al., "Passive detection and imaging of human body radiation using an uncooled field-effect transistor-based THz detector," *Sensors*, vol. 20, p. 4087, Jul. 2020.
[66] S. Malz, R. Jain, and U. R. Pfeiffer, "Towards passive imaging with CMOS THz cameras," in *Proc. Int. Conf. Infrared, Millimeter, Terahertz Waves*, 2016, pp. 1–2.
[67] K. Ikamas et al., "Quasi optical THz detectors in si CMOS," in *Proc. 2018 22nd Int. Microw. Radar Conf. (MIKON)*, 2018, pp. 719–721.
[68] G. Karolyi, D. Gergelyi, and P. Foldesy, "Sub-THz sensor array with embedded signal processing in 90 nm CMOS technology," *IEEE Sens. J.*, vol. 14, no. 8, pp. 2432–2441, Aug. 2014.
[69] S. Boppel et al., "CMOS integrated antenna-coupled field-effect transistors for the detection of radiation from 0.2 to 4.3 THz," *IEEE Trans. Microw. Theory Techn.*, vol. 60, no. 12, pp. 3834–3843, Dec. 2012.
[70] M. Ferreras, D. Čibiraitė Lukenskienė, A. Lisauskas, J. Grajal, and V. Krozer, "Broadband sensing around 1 THz via a novel biquad-antenna-coupled Low-NEP detector in CMOS," *IEEE Trans. THz Sci. Technol.*, vol. 11, no. 1, pp. 16–27, Jan. 2021.
[71] M. Andree, J. Grzyb, B. Heinemann, and U. Pfeiffer, "A D-band to J-band low-noise amplifier with high gain-bandwidth product in an advanced 130 nm SiGe BiCMOS technology," in *Proc. 2023 IEEE Radio Freq. Integr. Circuits Symp. (RFIC)*, pp. 137–140.
[72] A. Gadallah, M. H. Eissa, T. Mausolf, D. Kissinger, and A. Malignaggi, "A 300-GHz low-noise amplifier in 130-nm SiGe SG13G3 technology," *IEEE Microw. Wireless Compon. Lett.*, vol. 32, no. 4, pp. 331–334, Apr. 2022.
[73] H. Rücker and B. Heinemann, "High-performance SiGe HBTs for next generation BiCMOS technology," *Semicond. Sci. Technol.*, vol. 33, Sep. 2018, Art. no. 114003.
[74] G. Niu, "Noise in SiGe HBT RF technology: Physics, modeling, and circuit implications," in *Proc. IEEE*, vol. 93, no. 9, pp. 1583–1597, Sep. 2005.
[75] B. Heinemann, A. Fox, and H. Rücker, "Advanced transistor architectures for half-terahertz SiGe HBTs," *ECS Trans.*, vol. 50, pp. 61–71, 2013.
[76] B. Heinemann et al., "SiGe HBT technology with ft/fmax of 300 GHz/500 GHz and 2.0 ps CML gate delay," in *Proc. 2010 Int. Electron Devices Meeting (IEDM)*, Dec. 2010, pp. 30.5.1–30.5.4.
[77] H. Rücker, B. Heinemann, and A. Fox, "Half-terahertz SiGe BiCMOS technology," in *Proc. 2012 IEEE 12th Topical Meeting Silicon Monolithic Integr. Circuits RF Syst.*, Santa Clara, CA, USA, Jan. 2012, pp. 133–136.
[78] N. Rinaldi and M. Schröter, *Silicon-Germanium Heterojunction Bipolar Transistors for mm-Wave Systems: Technology, Modeling and Circuit Applications*. Denmark: River Publishers, 2018.
[79] B. Heinemann et al., "SiGe HBT with f_T/f_{max} of 505 GHz /720 GHz," in *Proc. IEEE Int. Electron Devices Meeting*, San Francisco, CA, USA, 2016, pp. 3.1.1–3.1.4.
[80] M. Schroeter and A. Chakravorty, "Compact hierarchical bipolar transistor modeling with HiCUM," in *International Series on Advances in Solid State Electronics and Technology*, Singapore: World Scientific, 2010.
[81] J. D. Cressler, "SiGe HBT technology: A new contender for Si-based RF and microwave circuit applications," *IEEE Trans. Microw. Theory Techn.*, vol. 26, no. 5, pp. 572–589, May 1998.
[82] M. Seif et al., "Study of low frequency noise in advanced SiGe:C heterojunction bipolar transistors," in *Proc. 44th IEEE Europ. Solid State Dev. Res. Conf. (ESSDERC)*, Venice, Italy, Sep. 2014, pp. 373–376.
[83] M. Bouhouche, S. Latreche, and C. Gontrand, "Low frequency noise in SiGe bipolar transistor: Effect of extrinsic base implantation traps," *Int. J. Comput. Appl.*, vol. 33, no. 6, pp. 59–64, Nov. 2011.
[84] S. P. O. Bruce, L. K. J. Vandamme, and A. Rydberg, "Measurement of low frequency base and collector current noise and coherence in SiGe heterojunction bipolar transistors using transimpedance amplifiers," *IEEE Trans. Electron Devices*, vol. 46, no. 5, pp. 993–1000, May 1999.
[85] C. Mukherjee et al., "Low-frequency noise in advanced SiGe:C HBTs–Part I: Analysis," *IEEE Trans. Electron Devices*, vol. 63, no. 9, pp. 3649–3656, Sep. 2016.
[86] C. Mukherjee et al., "Random telegraph noise in SiGe HBTs: Reliability analysis close to SOA limit," *Microelectron. Reliab.*, vol. 77, pp. 146–152, May 2017.
[87] J. Grzyb, R. Al Hadi, and U. Pfeiffer, "Lens-integrated on-chip antennas for THz direct detectors in SiGe HBT technology," in *Proc. 2013 IEEE Antennas Propag. Soc. Int. Symp. (APSURSI)*, 2013, pp. 2265–2266.
[88] J. Grzyb and U. Pfeiffer, "THz direct detector and heterodyne receiver arrays in silicon nanoscale technologies," *J. Infrared Millimeter Terahertz Waves*, vol. 36, no. 10, pp. 998–1032, Oct. 2015.
[89] J. Grzyb, B. Heinemann, and U. R. Pfeiffer, "A 0.55 THz near-field sensor with a μm-range lateral resolution fully integrated in 130 nm SiGe BiCMOS," *IEEE J. Solid-State Circuits*, vol. 51, no. 12, pp. 3063–3077, Dec. 2016.
[90] C. A. Balanis, *Antenna theory: Analysis and design*, John Wiley & Sons, 2005.
[91] C. S. Guenzer, "Chopping factors for circular and square apertures," *Appl. Opt.*, vol. 15, no. 1, pp. 80–83, Jan. 1976.
[92] Y. Touloukian and D. DeWitt, *Thermal Radiative Properties: Nonmetallic Solid*. New York, NY, USA: Springer, 1972.

Marcel Andree (Member, IEEE) received the M.Sc. degree and Ph.D. degree (passed with honours) in electrical engineering from the University of Wuppertal, Wuppertal, Germany, in 2017 and 2023, respectively, where he focused on the development and optimization of integrated mixed signal circuits and silicon-integrated circuits for THz imaging applications.

Since 2017, he has been a Staff Member with the Institute for High-Frequency and Communication Technology (IHCT), Wuppertal. His research interests include terahertz integrated circuit and system design in silicon technologies.

Janusz Grzyb received the M.Sc. degree (cum laude) in electronic engineering (with a major in the synthesis and design of analog CMOS and BiCMOS circuits with an individual study program) from the integrated Circuits Laboratory, Gdansk University of Technology, Gdansk, Poland, in 1998, and the Ph.D. degree from the Swiss Federal Institute of Technology, Zurich, Switzerland, in 2004.

In 1999, he joined Electronics Labs, SwissFederal Institute of Technology, Zurich, where he performed pioneering work in the area of low-cost large-area panel processing multichip-module-based system in package solutions for 60-GHz, 77-GHz, and 94-GHz applications. From 1998–1999, he was a Research Assistant with the Gdansk University of Technology. From 2004–2006, he was with the Communication System Design and High-Speed/Optical Packaging Groups, IBM T. J. Watson Research Center, Yorktown Heights, NY, USA, where he was involved in the development of the low-cost packaged highly integrated SiGe transceiver for 60-GHz Gb/s wireless data communication. From 2006–2009, he was with the Research and Development Group, Huber&Suhner, Pfaffikon ZH, Switzerland, where he brought onto the market one of the world's first commercially available point-to-point 60-GHz links: The Sensity Link System. Since 2009, he has been with the Institute for High-Frequency and Communication Technology, University of Wuppertal, Wuppertal, Germany. His current research interests include all aspects of silicon-integrated THz electronics.

Dr. Grzyb was a co-recipient of the 2006 Lewis Winner Award for Outstanding Paper of the IEEE International Solid-State Circuit Conference, the 2006 IBM Pat Goldberg Memorial Best Paper Award, the 2012 and 2018 Jan Van Vessem Award for Outstanding European Paper of the IEEE International Solid-State Circuits Conference, the 2014 Best Paper Award of the European Conference on Antennas and Propagation, and the Microwave Prize 2017 of the IEEE Microwave Theory and Techniques Society.

Holger Rücker received the diploma and Ph.D. degree in physics from the Humboldt University of Berlin, Berlin, Germany, in 1986 and 1988, respectively.

From 1989 to 1991, he was a Staff Member of the Humboldt University of Berlin. From 1991 to 1992, he was with the Max Planck Institute for Solid State Research, Stuttgart, Germany. He joined the Innovations for High Performance Microelectronics (IHP), Frankfurt (Oder), Germany, in 1992, where he is engaged in research on the physics and fabrication of semiconductor devices. He led the development of IHP's 130-nm SiGe BiCMOS technologies SG13S, SG13G2, and SG13G3. His research interests include SiGe bipolar devices, the development of CMOS and BiCMOS technologies, and their application in radio-frequency integrated circuits.

Ullrich R. Pfeiffer (Fellow, IEEE) received the diploma degree and Ph.D. degree in physics from the University of Heidelberg, Heidelberg, Germany, in 1996 and 1999, respectively.

In 1997, he worked as a Research Fellow with the Rutherford Appleton Laboratory, Oxfordshire, England. From 1999–2001, he worked as a Postdoctoral Researcher with the University of Heidelberg, on real-time electronics for particle physics experiments and with the European Organization for Nuclear Research (CERN), Geneva, Switzerland. From 2001–2006, he was with the IBM T.J. Watson Research Center, Yorktown Heights, NY, USA, where his research involved RF circuit design, power amplifier design at 60 GHz, and 77 GHz, high-frequency modeling, and packaging for millimeter-wave communications systems. His current research interests include silicon RFICs for mmWave/THz communications, radar, and imaging systems.

Dr. Pfeiffer was a recipient of a European Young Investigator Award in 2007 and led the THz electronics group at the Institute of High-Frequency and Quantum Electronics at the University of Siegen, Siegen, Germany, and the co-recipient of the 2004 and 2006 Lewis Winner Award for Outstanding Paper at the IEEE International Solid-State Circuit Conference, the co-recipient of the 2006 IBM Pat Goldberg Memorial Best Paper Award, the 2008 EuMIC Best Paper Award, the 2010 EuMC Microwave Prize, the 2014 EuCAP Best Paper Award, the 2017 Microwave Prize, and the 2012 and 2018 Jan Van Vessem Award for Outstanding European Paper at the IEEE International Solid-State Circuit Conference. Since 2008, he has been holding the High-Frequency and Communication Technology chair at the University of Wuppertal, Wuppertal, Germany. He has been a Distinguished Lecturer for the IEEE Solid-State Circuits Society and the President of the German Association for Electrical Engineering and Information Technology e.V. (FTEI).